Single particle zeta-potential measurements reveal the role of electrostatics in protein condensate stability

Timothy J. Welsh[a,1], Georg Krainer[a,1], Jorge R. Espinosa[b,1], Jerelle A. Joseph[b], Akshay Sridhar[b], Marcus Jahnel[c,d,e], William E. Arter[a], Kadi L. Saar[a], Simon Alberti[d,*], Rosana Collepardo-Guevara[b,f,g,*], Tuomas P.J. Knowles[a,b,*]

[a] Centre for Misfolding Diseases, Department of Chemistry, University of Cambridge, Lensfield Road, Cambridge CB2 1EW, UK

[b] Cavendish Laboratory, University of Cambridge, J J Thomson Avenue, Cambridge CB3 0HE, UK

[c] Max Planck Institute of Molecular Cell Biology and Genetics, Pfotenhauerstr. 108, 01307 Dresden, Germany

[d] Biotechnology Center (BIOTEC), Center for Molecular and Cellular Bioengineering (CMCB), Technische Universität Dresden, Tatzberg 47/49, 01307 Dresden, Germany

[e] Cluster of Excellence "Physics of Life", TU Dresden, Dresden, Germany

[f] Department of Genetics, University of Cambridge, Cambridge CB2 3EH, UK

[g] Department of Chemistry, University of Cambridge, Lensfield Road, Cambridge CB2 1EW, UK

* To whom correspondence may be addressed: Tuomas P.J. Knowles (tpjk2@cam.ac.uk), Rosana Collepardo-Guevara (rc597@cam.ac.uk), Simon Alberti (simon.alberti@tu-dresden.de)

[1] These authors contributed equally

Keywords: liquid–liquid phase separation, microfluidics, FUS, zeta potential, emulsion

Author Contributions: T.J.W., G.K., and T.P.J.K. conceived of the idea and designed research. T.J.W. carried out all microfluidic experiments and analyzed the data. J.R.E., J.A.J., A.S., and R.C.G. designed the simulations. J.R.E. and J.A.J. performed the coarse-grained simulations. A.S. performed the atomistic simulations. J.R.E., J.A.J., and A.S. analyzed the simulation results. M.J., T.J.W., and G.K. performed and analyzed optical tweezer experiments. R.C.G. supervised the simulation work. W.E.A. and K.L.S. provided microfluidics chip designs and data analysis approaches. S.A. provided protein materials. T.J.W. and G.K. wrote the manuscript. All authors edited the manuscript.

This PDF file includes:

Main Text
Figures 1 to 5
Supporting information
Figures S1 to S7
Table S1

Abstract

Liquid–liquid phase separation underlies the formation of biomolecular condensates and membraneless compartments in living cells. Physically, condensed liquid biomolecular systems represent water-in-water emulsions with a very low surface tension. Such emulsions are commonly unstable towards coalescence, yet in order to be functional, they must persist inside the cell. This observation thus raises the fundamental question of the origin of the stability of such emulsions, and whether passive physical mechanisms exist that stabilize droplets against fusion or coalescence. Here, through measurement of condensate zeta potentials on a single droplet level, we show that surface electrostatic properties of condensates can be used to describe and assess the emulsion stability of condensed liquid biomolecular systems. We find that condensates formed from a representative set of peptide/nucleic acid and protein systems have zeta potentials in the stability range predicted by classical colloid theory. Specifically, we describe the electrostatic nature of PR_{25}:PolyU and FUS condensates and show that their zeta potentials correlate well with their propensity to fuse, coalesce, and cluster. Further, we bring together experiments with multiscale molecular simulations and demonstrate that the differences in zeta potential and subsequent stability of biomolecular condensates are modulated by their internal molecular organization. Taken together, these findings shed light on the origin of the stability of biomolecular condensate systems, and connect the organization of molecular-level building blocks to the overall stability of phase-separated biomolecular systems.

Significance Statement

Biomolecular condensation is a phenomenon involved in the subcellular organization of living systems, yet little is known about the molecular forces that underlie their stability. Condensates consist of a biopolymer-rich phase dispersed as microdroplets in a polymer-poor continuous phase. Both phases are aqueous and, as such, the surface tension between them is low. However, how condensates are stabilized and maintain their integrity has remained unknown. Here we use a microfluidic platform to analyze the zeta potentials of condensates and show that they fit within the stability range of classical colloids. Furthermore, condensate zeta potentials correlate well with their propensity to fuse and coalesce, suggesting that emulsion theory is a new lens through which biomolecular condensation can be viewed and studied.

Introduction

Solutions of macromolecules such as proteins, peptides, and nucleic acids can undergo demixing through liquid–liquid phase separation (LLPS). This phenomenon results in the formation of condensed liquid microenvironments (i.e., biomolecular condensates), which are dispersed in a dilute aqueous phase (*1–3*). LLPS underlies the formation of membraneless organelles in living cells and provides a mechanism for the spatiotemporal (*4*) control of several vital processes within cells (*5*), including RNA processing and stress signaling (*6*, *7*). LLPS-driven processes have further been linked to several pathological processes related to diseases and aging underscored by liquid-to-solid transitions (*8–10*).

Although numerous biological systems have been shown to undergo LLPS, only a few molecular determinants for phase separation behavior have been identified to date, and even less is known regarding how these dynamic assemblies are stabilized against coalescence; an essential factor to ensure their functionality *in vivo*. Biomolecular condensates *in vivo* can remain stable for varying periods of time that range from seconds to hours, which is intricately linked to their biological function (*7*, *11*). Whilst active chemical and biological processes in cells have been suggested to confer stability (*12*), observations *in vitro* imply that there likely exist inherent passive stabilization mechanisms that prevent condensates from rapidly fusing and clustering.

Intermolecular local electrostatic forces are one of the key drivers of phase separation (*13*). A range of polyelectrolytes can be used to assemble peptides and proteins into condensates *in vitro*, independent of any conserved hydrophobic, hydrophilic, aromatic, or biologically specific properties of the polyelectrolytes (*14*). It has also been shown that modulating salt concentration has a direct effect on the ability of proteins to undergo LLPS (*15*). Based on the role of electrostatics, we hypothesized that condensates are stable water-in-water emulsions similar to other polyelectrolyte coacervate systems, and stability against fusion and clustering may be electrostatically driven.

The specific quantity of interest to assess such stability is the zeta potential, the electro-kinetic potential at the edge of the interfacial double layer coating the surface of any charged particle (Figure 1A) (*16*). The zeta potential has long been used to describe the stability of emulsions and colloids against coalescence, coagulation, and clustering (*17*). In particular, low zeta potentials, usually smaller than 30 or 40 mV in absolute value, tend to be associated with instability (*18*, *19*). Outside this regime, electrostatic repulsion results in stability against fusion.

Here we explore the role of surface electrostatics in the stabilization of condensates through measurements of their zeta potential. To this effect, we devised a microfluidic approach that enables high-throughput measurement of zeta potentials at the resolution of individual condensates. We show that zeta potentials obtained for various biomolecular condensates correlate well with their propensity to fuse, coalesce, and cluster. These results, together with insights from molecular dynamics simulations, establish the zeta potential as a fundamental quantity to infer the stability of biomolecular condensates from an intrinsic property of the system.

Results

The sizes of biomolecular condensates are typically highly heterogeneous. Therefore, to quantify the zeta potential of biomolecular condensates experimentally, we developed a high-throughput single-particle microfluidic approach based on free-flow electrophoresis (μFFE), using a 3D microfluidic device, that enables in-solution quantification of zeta potentials with single-droplet resolution (Figure 1B-D). μFFE has been previously used for the measurement of protein charge (*20*, *21*) and the separation of proteins and nucleic acids (*22*), and relies on the flow of an analyte through a measurement chamber while an electric field is applied perpendicular to the flow direction. Here we adapted this technique for single-droplet zeta potential measurements, which allows us to study condensates and their zeta potentials in solution without any surface interactions. The experimental approach is illustrated in Figure 1B–E. After condensates are injected into the μFFE microfluidic device (Figure 1B), they move in response to the applied voltage (Figure 1C, left), and their positions are recorded as a measure of electrophoretic mobility, as shown in Figure 1C, right panel. Once positions of individual droplets are quantified from the fluorescence images, the zeta potential can be directly obtained, as further described in the Supporting Methods. In this manner, zeta potential distributions from measurement of thousands of individual condensates can be obtained within a few minutes (Figure 1D). This approach thus allows for the high-resolution quantification of zeta potentials at the single-particle level, which is especially important for samples that are poly-dispersed both in zeta potential and size as is the case for liquid biomolecular condensates.

With the μFFE approach, zeta potential measurements were acquired for three different biomolecular condensate systems. We first focused on a dipeptide repeat derived from the hexanucleotide repeat expansion in the chromosome 9 open reading frame 72 (*C9orf72*) gene, implicated in amyotrophic lateral sclerosis (ALS) (*23*, *24*). The peptide used consisted of 25 repeats of the dipeptide proline-arginine (PR_{25}). This type of peptide is well known to phase separate in response to negatively charged polymers (*2*, *24*), including single-stranded RNA consisting of 2500–3500 bases (molecular weight from 800–1000 kDa) of uridine (PolyU). In addition to PR_{25}, the protein fused in sarcoma (FUS) was studied. FUS is a widely expressed RNA-binding protein that has been shown to phase separate and has been correlated with ALS phenotypes (*25–27*). We also studied a disease related mutant FUS G156E, which is known to have a faster transition from the liquid-condensed state to the solid state (*8*). Both FUS variants were expressed with a C-terminal EGFP fluorescent protein tag for visualization purposes.

Each of the phase separating systems was assessed using μFFE in order to determine zeta potential distributions from thousands of individually probed biomolecular condensates. Figure 2 shows the range of obtained zeta potentials across the different protein condensates, as given by their mean values (μ), and their degree of heterogeneity, as assessed by the standard deviation of the distributions (σ). The trend of absolute zeta potentials of the condensates from largest to

smallest was PR_{25}:PolyU > FUS wild type > FUS G156E, with mean zeta potential values ranging from –40.6 mV to –15.0 mV. The distributions also showed that the condensates are poly-dispersed in zeta potential, as evident by standard deviations around 11–13 mV. Further analysis showed that the condensate systems are poly-dispersed in size; yet there is no distinct correlation between zeta potential and size (Figure S3).

Since the zeta potential is a fundamental parameter that modulates the long-range repulsion between colloidal particles in solution and therefore delineates the stability of emulsions against coalescence or fusion and clustering, we hypothesized that the trend observed for the different systems could reflect the stability of condensates. Indeed, results from epifluorescence microscopy suggest that there is a correlation between zeta potential and condensate stability (Figure 3A–E). Specifically, PR_{25}:PolyU condensates remain stable over hours as has been previously reported (*24*), whereas FUS wild type and FUS G156E condensates rapidly fuse, cluster, and wet surfaces.

To corroborate these observations, we further conducted controlled fusion experiments using dual-trap optical tweezers (*8*, *13*) (Figure 4). In these experiments, PR_{25}:PolyU condensates showed a higher resistance against fusion compared to FUS wild type condensates. Whereas FUS condensates fused immediately upon contact, PR_{25}:PolyU condensates required an additional force to initiate a fusion event, indicating the presence of a repulsion between the condensates. This characteristic is evident in images of moderately deformed PR_{25}:PolyU droplets just before fusion, and in the force measurements from optical tweezer experiments (Figure 4A). Here, we observed a dip in the laser signal just before PR_{25}:PolyU droplet fusions, indicative of an increased repulsive force between the droplets. This feature was absent in FUS wild type condensates. These observations correlate with the observations that PR_{25}:PolyU condensates had a greater absolute zeta potential compared to FUS, and thus shows that a greater zeta potential indeed correlates with an increased barrier to fusion. Interestingly, although there seems to be a higher energy barrier to initiate droplet fusion in PR_{25}:PolyU condensates (Figure 4B, bottom panel), once started, fusion proceeds much faster for PR_{25}:PolyU condensates than for FUS wild-type condensates (Figure 4B, top panel), suggesting that there is no correlation between the barrier to fusion and the fusion rate.

To understand the molecular origin of the measured zeta potential values and explore whether or not they correlate with variations in the molecular organization within the condensates, in particular the spatial distribution of charged groups, we developed a two-step multiscale molecular simulation approach that exploits the advantages of coarse-grained and all-atom models. In a first step, we analyzed the molecular organization of FUS and PR_{25}:PolyU condensates by means of direct coexistence simulations of tens to hundreds of interacting biomolecules using the sequence-dependent LLPS coarse-grained model of the Mittal group (*28*). In a second step, we performed a back-mapping procedure to convert equilibrium coarse-grained condensates into fully atomistic systems, including explicit solvent and ions, and investigate differences in the absorption and distribution of ions between the condensed and dilute phase in both systems. Such a multiscale

procedure is necessary because, on the one hand, investigating the self-organization of proteins into condensed liquids is only feasible with coarse-grained models given the large system sizes and long timescales required, and on the other hand, capturing changes in counterion behavior requires an explicit all-atom description of biomolecules, solvents, and ions.

Our simulations reveal a striking difference in the molecular organization of FUS and PR_{25}:PolyU condensates (Figure 5). Due to the highly symmetric and charge-patterned sequences of PR_{25} and PolyU and their LLPS being mainly enabled by electrostatic Arg:U interactions, we find a uniform distribution of all species (U, Pro, Arg), throughout the PR_{25}:PolyU condensates (Figure 5; PR_{25}:PolyU). In contrast, FUS condensates exhibit a remarkable heterogeneous yet symmetric molecular organization (Figure 5; FUS) that resembles a micelle-like structure with a hydrophobic-rich amino acid core and a more charge-dense edge (see positional distribution of FUS domains in Figure S5).

The structural heterogeneity of FUS can be rationalized from its diverse sequence composition. From the point of view of LLPS, the 526-residue FUS can be partitioned into an uncharged disordered prion-like domain (PLD) enriched in Gln, Gly, Ser, and Tyr (residues 1–165), three positively charged disordered Arg-Gly-Gly (RGG) rich regions (RGG1: residues 166–267, RGG2: residues 371–421, and RGG3: residues 454–526), and two globular regions (a RNA-recognition motif: residues 282–371, and a zinc finger: residues 422–453) (*29*). We find that FUS condensates are most strongly stabilized both by electrostatic cation–π interactions between the charged RGG1 region and the Tyr-rich PLD, and by PLD–PLD hydrophobic interactions, and more modestly by interactions involving the other domains (Figure S6). These patterns of interactions favor immersion of the RGG1s and PLDs deep into the condensate and position the less LLPS-active RGG2-3 and globular domains towards the surface (Figure S5). Accordingly, the surface of FUS condensates is rich in charge (Figure 5C; FUS), relative to the core which is more tightly held together by hydrophobic and cation–π interactions.

Hence, combining our simulation results and the experimental zeta potential measurements, our findings suggest that larger absolute zeta-potential values are observed in systems where LLPS is more heavily driven by electrostatics. Furthermore, at physiological salt concentrations, the formation of attractive electrostatic interactions leads to a greater enthalpic gain than hydrophobic interactions, further supporting the notion that PR_{25}:PolyU condensates (purely electrostatic interactions) are more stabilized than FUS condensates (mixed electrostatic and hydrophobic interactions). Therefore, larger zeta potential values are likely to be correlated with stronger intermolecular interactions and may make the condensates most stable in response to changing environments such as temperature, pH, or chemical modifications.

Our atomistic MD simulations (Figure 5D) reveal additional molecular determinants underlying the greater zeta potential values of PR_{25}:PolyU. Besides their notably higher density of charged species (Figure 5B,C; left), PR_{25}:PolyU condensates establish more favorable electrostatic

interactions with counterions than FUS condensates. This observation implies an increased ability of PR_{25}:PolyU to sequester counterions from the diluted phase and to concentrate them in the condensate (Figure S7A) relative to FUS, and, importantly, to reduce the mobility of such counterions once they enter the condensed phase (Table S1). In agreement with this idea, FUS condensates are more depleted of charged amino acids (Figure 5B,C; right), which results in a lower concentration of counterions within the condensates. Thus, in FUS, ions preferentially localize at the surface (Figure S7B) and diffuse more freely across the condensate (Table S1). The increased surface density of counter ions directly results in further charge screening and reduced zeta potential, as is consistent with our experimental observations.

The wide variations in condensate zeta potential values measured experimentally are indicative of surface heterogeneity, both in shape and charge distribution. This notion is supported by our simulations, which reveal a highly dynamical behavior of biomolecules inside condensates. Specifically, biomolecules within liquid condensates sample a wide range of conformations and interconnect with one another through weak short-lived bonds, forming a random and dynamical percolated network. Importantly, in such networks, biomolecules (which are the nodes of the network) can easily exchange locations and binding partners. Hence, our data suggests that charge and geometric heterogeneities may arise from dynamic rearrangements of the constituent biomolecules of condensates.

Discussion

Through the development of a μFFE approach for probing electrophoretic properties of phase-separated condensates, we were able to quantify the zeta potential of biomolecular condensates with single-droplet resolution and correlate this parameter of emulsion stability to condensate stability. Our results show that PR_{25}:PolyU condensates have a higher zeta potential than FUS wild type and G156E mutant condensates, and this trend correlates well with qualitative stability observations from microscopy experiments and quantitative data from optical tweezer measurements. Through multiscale MD simulations, we show that the differences in zeta potential (and subsequent stability of biomolecular condensates) emerges from distinctly different molecular organizations within the condensates. While PR_{25}:PolyU condensates are stabilized by electrostatic interactions, which are largely homogeneously distributed and possess highly charged surfaces, FUS droplets are distinctly heterogeneous, predominantly sustained by cation–π and hydrophobic interactions and exhibit charged interfaces, though to a lesser extent than PR_{25}:PolyU. These findings, therefore, establish the zeta potential as a fundamental quantity to infer passive stability of biomolecular condensates from an intrinsic property of the system and give a path to describe biomolecular condensates as ‘passive emulsions’.

An important question regarding the observation of the stability of condensates against coalescence *in vivo* is whether this stability originates from their nature as ‘active emulsions’ (*12*,

30) or whether passive mechanisms, as studied here, are sufficient to explain the observed stability. The active nature of the condensates has been proposed to originate from two possible factors: either the continual flux of protein both in and out of the condensates or the catalytic activity within condensates producing molecules, which then incorporate into the condensates themselves. In order to evaluate the role of such active processes, it is crucial to understand the contribution of passive mechanisms; indeed, a certain level of emulsion stability has been shown for both FUS (*8*, *15*) and PR_{25} (*24*, *31*) in the absence of any active or catalytic processes suggesting that passive processes are involved. Our results provide a simple framework for conferring passive stability to biomolecular condensates stemming from electrostatic effects. Such a passive stabilization could either be caused by the repulsive forces between condensates or could stem from effects that surface electrostatics have on the surface tension of the emulsion. Previous studies suggest that surface charge of emulsions can have a direct effect on the surface tension (*32*, *33*). The latter has been shown to increase with increasing ionic strength, which in turn decreases the zeta potential (*34*, *35*). These results together with our observations herein therefore suggest that larger zeta potentials may lower the surface tension of a condensate and thus result in its stabilization.

The correlation between electrostatic properties and stability, as predicted by classical emulsion theory, provides a means by which protein condensates can be classified and compared according to their zeta potential. A larger absolute value of zeta potential confers greater resistance against coalescence and clustering (*18*, *36*). Moreover, a limiting value for the two condensate systems studied here seems to exist around the –30 mV threshold that has been previously put forward in literature (*17*, *19*), meaning that absolute zeta potentials greater than 30 mV confer stability and values less than 30 mV suggest increased propensity for clustering and coalescence. Along with this cut-off, the significant variability in zeta potential, evident by the wide distributions, indicates that a single ensemble of condensates will have varied degrees of stabilization within it. The measurement of zeta potentials also revealed that the surfaces of condensates possess markedly different surface charges. Our multiscale molecular simulations further reveal that greater absolute zeta potential values are consistent with more highly charged surfaces and higher internal absorption of counterions. These results offer a deeper understanding of the internal and surface geometry of condensates.

A further observation is that the zeta potentials of biomolecular condensates can considerably vary even though their overall composition remains constant. This variation is indicated by the large standard deviations for the zeta potential distributions, which ranged from 24% to 78% of the mean, while the standard errors were all well below 0.1% due to the large sample size. Thereby, further suggesting that heterogeneity with respect to surface geometry is present across condensates within a single sample, which may be partly due to dynamic rearrangement and exchange of proteins both within the condensates and with the exterior. This constant reassembly is consistent with the description of condensates as highly dynamic assemblies (*26*, *37*). Our MD simulations

also reveal the highly dynamical nature of the condensates. Specifically, biomolecules adopted diverse conformations and, due to weak intermolecular interactions, dynamically switched their interaction to other neighbors. In some cases, proteins even escaped to the diluted phase and were subsequently recruited back into the condensate, thereby changing the shape and chemical composition of the interface continuously. Indeed, the ability of biomolecules to form a large number of weak interconnections within a random and dynamical percolated network is critical to the stability of biomolecular condensates.

The observed correlation between stability and zeta potential also has important pathophysiological implications, specifically for the transition of condensates from their liquid state to solid aggregates. It has been shown that FUS can transition into toxic aggregates associated with the onset and development of motor neuron disease more readily when it is contained in condensates (*8*), and this trend holds true for other proteins as well, including TDP-43 and other condensate forming systems (*38*, *39*). Recent theoretical work has also highlighted how condensates could behave as compartments for aggregate formation, and has even indicated how more aggregates could form within condensates of greater size (*40*). In addition, it is well known that the primary nucleation of solid phases is directly dependent on the number of available precursor monomer protein molecules (*41*) and, since monomer concentration is higher in condensates than in the dilute phase (*42*), it is evident that condensates may serve as epicenters for the formation of toxic solid aggregates. Hence, the propensity of FUS condensates to more readily fuse, as dictated by a low zeta potential, causes the condensates to grow bigger over time. This larger size may render them more favorable for nucleation and growth of aggregates. Furthermore, the lower zeta potential observed for FUS G156E compared to FUS wild type might serve to explain its higher propensity to form aggregates (*8*).

Beyond pathophysiological implications, the stability and size control of phase separated condensates has been indicated to be relevant particularly in the control of the size of organelles during cell growth and embryonic development (*43*, *44*). Additionally, the size of condensates has been linked to the rapidity of cancer proliferation (*45*), suggesting that the modulation of the size of certain condensates, controlled through their zeta potential, could be a route for therapeutic interventions.

Taken together, this work establishes the zeta potential as a fundamental quantity to infer stability of biomolecular condensates. By probing the zeta potential on a single condensate level, we were able to elucidate the electrostatic nature of PR_{25}:PolyU and FUS condensates and correlate these experimental results with their observed stability. Computational studies further described the interior geometry of these condensates and showed how the symmetric vs asymmetric distribution of charges within condensates are correlated with the intermolecular interactions of their component biomolecules. Overall, these results help provide an understanding

of the physical factors that can control condensate stability and confer protection against droplet fusion.

Materials and Methods

Materials. All reagents and chemicals were purchased with the highest purity available. The PR_{25} peptide, containing 25 proline–arginine repeats, was obtained from GenScript. N-terminally labelled PR_{25} was obtained by reacting the peptide with amine-reactive AlexaFluor546 (Sigma-Aldrich). PolyU RNA with a molecular weight range from 800–1,000 kDa was purchased from Sigma-Aldrich. FUS wild type and FUS G156E were produced as C-terminal EGFP fusion proteins as previously described (*8*) and stored in 50 mM Tris-HCl (pH 7.4), 500 mM KCl, 1 mM dithiothreitol, 5% glycerol. PR_{25} phase separation was induced by mixing 100 µM PR_{25} peptide with 1 mg/mL PolyU RNA in 5 mM Tris-HCl (pH 7.4). For both FUS variants, phase separation was induced by diluting the proteins to a final protein concentration of 3 µM in 25 mM KCl, 5 mM TRIS (pH 7.4). For PR_{25}:PolyU and both FUS mutants, the phase separated condensates were analyzed via µFFE within ~10 min of creation in order to minimize ageing effects; no systematic differences in zeta potential were observed across replicate samples on this time scale. 60 nm fluorescently labelled spherical gold nanoparticles (NanoPartz) were used for control measurements mentioned in Figure S4.

µFFE experiments. The design of the 3D µFFE microfluidic chip with liquid electrodes was adapted from a device previously used for studying protein charge and the separation of biomolecules (*20*, *22*). A schematic is shown in Figure S1. The device, constructed from a top and a bottom layer, was fabricated using standard single- and multilayer photolithography techniques as described in detail in the Supporting Information. Briefly, the microfluidic channels within each layer were patterned into polydimethylsiloxane (PDMS; Sylgard184, Dow Corning) using SU-8 photoresist (Microchem) on silicon masters (MicroChemicals). Top and bottom PDMS layers were then connected through plasma bonding and subsequently bonded to glass microscope slides using oxygen plasma (Diener Electronics). Devices were operated as detailed in the Supporting Information and fluids introduced using automated syringe pumps (neMESYS, Cetoni). Electric potentials were applied using a programmable 500 V power supply (Elektro-Automatik EA-PS 9500-06) and images acquired using a Zeiss AxioObserver D1 microscope. Further details are given in the Supporting Information. Image and data analysis were performed using the Fiji/ImageJ data processing software and custom-written Python scripts, respectively. Zeta potentials were calculated as described in detail in the Supporting Information.

Epifluorescence and phase-contrast microscopy in droplet stability experiments. For experiments assessing condensate stability, epifluorescence and phase contrast images were captured using an AxioObserver D1 microscope (Zeiss) with either a 40x or 100x air objective after

the specified aging time for each sample (Figure 3). Condensates were imaged within a 50 µm tall microfluidic imaging chamber in the same buffer conditions as utilized for µFFE experiments.

Optical tweezer measurements. Condensates were phase-separated in 5 mM Tris-HCl, 25 mM KCl, pH 7.4 and immediately applied to a sample chamber. Two droplets were trapped in two optical traps of the same trap stiffness. With the first trap stationary, the second trap was moved to bring the droplets into contact and initiate fusion. If fusion did not occur upon first contact as in the case of PR_{25}:PolyU condensates, the second trap was further moved to push the droplets together. As soon as coalescence initiated, the traps were kept stationary. Laser signals were recorded at 1 kHz resolution. Signals from the two traps, equal in magnitude and opposite in sign, were combined into the differential signal, from which coalescence relaxation times were deduced. A random sample of 5% of the recorded data is plotted as grey points in Figure 4. Raw data were smoothed with a Savitzky-Golay filter of 3rd order and a window of 501 points.

Fit of optical tweezer traces. The standard model for droplet fusion is based on the assumption that droplets start to coalesce as soon as their surfaces touch. This assumption holds true for many purified protein liquids (*8*, *13*, *46*, *47*). To characterize fusion dynamics, time traces of the tweezer signal, *S*(*t*), were fitted with a stretched exponential model as described previously (*13*). Briefly, the model is defined as:

$$S(t) = \begin{cases} S_{\text{offset}}, & \text{if } t < t_{\text{start}} \\ S_{\text{offset}} + (S_{\text{plateau}} - S_{\text{offset}}) \cdot [1 - \exp(-\frac{t - t_{\text{start}}}{\tau})^{\beta}], & \text{if } t \geq t_{\text{start}} \end{cases}$$

where τ denotes the relaxation time, β the stretch exponent, t_{start} the onset of fusion, S_{offset} the signal offset on the detector, and S_{plateau} the final signal value after coalescence finished.

All fusion traces (Figure 4A) have been normalized and aligned according to the start time of coalescence as deduced from the fit. Residuals from the fit were calculated for the smoothed signal. We took the maximum negative deviation from the standard model within a window of 15 seconds before the onset of fusion as a proxy for the additional energy barrier to be overcome. To quantify the fusion dynamics, the mean relaxation time was normalized by the geometric radius of the two fusing droplets.

Multiscale molecular simulations. To investigate the molecular organization of proteins, PolyU and ions within the condensates, we develop a two-step multiscale molecular simulation method. The first step consists of coarse-grained MD simulations of tens to hundreds of biomolecules to investigate the equilibrium ensembles of FUS and PR_{25}:PolyU condensates (see further coarse-grained simulation details in the Supporting Information). During the second step, we undertake a back-mapping procedure and perform atomistic MD simulations with explicit solvent and ions to assess the distribution of ions in the condensed and diluted phases, and obtain magnitudes directly related to zeta potentials estimations (see details of atomistic simulations in the Supporting Information).

Acknowledgments

We thank members of the Knowles laboratory for discussions. The research leading to these results has received funding from the European Research Council (ERC) under the European Union's Seventh Framework Programme (FP7/2007-2013) through the ERC grant PhysProt (agreement no. 337969) (T.P.J.K.), under the European Union's Horizon 2020 Framework Programme through the Future and Emerging Technologies (FET) grant NanoPhlow (agreement no. 766972) (T.P.J.K., G.K.), under the European Union's Horizon 2020 Framework Programme through the Marie Sklodowska-Curie grant MicroSPARK (agreement no. 841466) (G.K.), and under the European Union's Horizon 2020 research and innovation programme through the ERC grant InsideChromatin (agreement no. 803326) (R.C.G.). We further thank the Newman Foundation (T.P.J.K.), the Biotechnology and Biological Sciences Research Council (T.P.J.K.), the Herchel Smith Funds of the University of Cambridge (G.K.), the Wolfson College Junior Research Fellowship (G.K.), the Winston Churchill Foundation of the United States (T.J.W.), the Harding Distinguished Postgraduate Scholar Programme (T.J.W.), the Winton Advanced Research Fellowship (R.C.G.), the Oppenheimer Research Fellowship (J.R.E.), the Roger Ekins Fellowship (J.R.E.), the King's College Research Fellowship (J.A.J.), the Engineering and Physical Sciences Research Council (K.L.S.), and the Schmidt Science Fellowship program in partnership with the Rhodes Trust (K.L.S.). The simulations were performed using resources provided by the Cambridge Tier-2 system operated by the University of Cambridge Research Computing Service (http://www.hpc.cam.ac.uk) funded by EPSRC Tier-2 capital grant EP/P020259/1. We thank Jeetain Mittal and Gregory L. Dignon for invaluable help with the implementation of their sequence-dependent protein coarse-grained model in LAMMPS.

Notes

The authors declare no competing interest.

References

1. S. Alberti, A. Gladfelter, T. Mittag, Considerations and Challenges in Studying Liquid-Liquid Phase Separation and Biomolecular Condensates. *Cell*. **176**, 419–434 (2019).

2. S. Boeynaems, S. Alberti, N. L. Fawzi, T. Mittag, M. Polymenidou, F. Rousseau, J. Schymkowitz, J. Shorter, B. Wolozin, L. Van Den Bosch, P. Tompa, M. Fuxreiter, Protein Phase Separation: A New Phase in Cell Biology. *Trends Cell Biol.* **28**, 420–435 (2018).

3. A. A. Hyman, C. A. Weber, F. Jülicher, Liquid-Liquid Phase Separation in Biology. *Annu. Rev. Cell Dev. Biol.* **30**, 39–58 (2014).

4. C. F. Lee, C. P. Brangwynne, J. Gharakhani, A. A. Hyman, F. Jülicher, Spatial Organization of the Cell Cytoplasm by Position-Dependent Phase Separation. *Phys. Rev. Lett.* **111**, 088101 (2013).

5. J. A. Riback, C. D. Katanski, J. L. Kear-scott, V. Evgeny, A. E. Rojek, T. R. Sosnick, D. A. Drummond, Tuned Response. *Cell*. **168**, 1028–1040 (2018).

6. M. Feric, N. Vaidya, T. S. Harmon, D. M. Mitrea, L. Zhu, T. M. Richardson, R. W. Kriwacki, R. V. Pappu, C. P. Brangwynne, Coexisting Liquid Phases Underlie Nucleolar Subcompartments. *Cell*. **165**, 1686–1697 (2016).

7. C. P. Brangwynne, C. R. Eckmann, D. S. Courson, A. Rybarska, C. Hoege, J. Gharakhani, F. Jülicher, A. A. Hyman, Germline P Granules Are Liquid Droplets That Localize by Controlled Dissolution/Condensation. *Science*. **324**, 1729–1732 (2009).

8. A. Patel, H. O. Lee, L. Jawerth, S. Maharana, M. Jahnel, M. Y. Hein, S. Stoynov, J. Mahamid, S. Saha, T. M. Franzmann, A. Pozniakovski, I. Poser, N. Maghelli, L. A. Royer, M. Weigert, E. W. Myers, S. Grill, D. Drechsel, A. A. Hyman, S. Alberti, A Liquid-to-Solid Phase Transition of the ALS Protein FUS Accelerated by Disease Mutation. *Cell*. **162**, 1066–1077 (2015).

9. S. Alberti, S. Carra, Quality Control of Membraneless Organelles. *J. Mol. Biol.* **430**, 4711–4729 (2018).

10. S. Alberti, A. A. Hyman, Are aberrant phase transitions a driver of cellular aging? *BioEssays*. **38**, 959–968 (2016).

11. S. Alberti, S. Saha, J. B. Woodruff, T. M. Franzmann, J. Wang, A. A. Hyman, A User's Guide for Phase Separation Assays with Purified Proteins. *J. Mol. Biol.* **430**, 4806–4820 (2018).

12. C. A. Weber, D. Zwicker, F. Jülicher, C. F. Lee, Physics of active emulsions. *Reports Prog. Phys.* **82**, 064601 (2019).

13. J. Wang, J. M. Choi, A. S. Holehouse, H. O. Lee, X. Zhang, M. Jahnel, S. Maharana, R. Lemaitre, A. Pozniakovsky, D. Drechsel, I. Poser, R. V. Pappu, S. Alberti, A. A. Hyman, A Molecular Grammar Governing the Driving Forces for Phase Separation of Prion-like RNA Binding Proteins. *Cell*. **174**, 688–699 (2018).

14. S. Boeynaems, A. S. Holehouse, V. Weinhardt, D. Kovacs, J. Van Lindt, C. Larabell, L. Van Den Bosch, R. Das, P. S. Tompa, R. V Pappu, A. D. Gitler, Spontaneous driving forces give rise to protein-RNA condensates with coexisting phases and complex material properties. *Proc. Natl. Acad. Sci.* **116**, 7889–7898 (2019).

15. S. Qamar, G. Z. Wang, S. J. Randle, F. S. Ruggeri, J. A. Varela, J. Q. Lin, E. C. Phillips, A. Miyashita, D. Williams, F. Ströhl, W. Meadows, R. Ferry, V. J. Dardov, G. G. Tartaglia, L. A. Farrer, G. S. Kaminski Schierle, C. F. Kaminski, C. E. Holt, P. E. Fraser, G. Schmitt-Ulms, D. Klenerman, T. Knowles, M. Vendruscolo, P. St George-Hyslop, FUS Phase Separation Is Modulated by a Molecular Chaperone and Methylation of Arginine Cation-π Interactions. *Cell*. **173**, 720--734.e15 (2018).

16. G. W. Lu, P. Gao, Emulsions and Microemulsions for Topical and Transdermal Drug Delivery. *Handb. Non-Invasive Drug Deliv. Syst.*, 59–94 (2010).

17. A. Wiącek, E. Chibowski, Zeta potential, effective diameter and multimodal size distribution in oil/water emulsion. *Colloids Surfaces A Physicochem. Eng. Asp.* **159**, 253–261 (1999).

18. J. N. Losso, A. Khachatryan, M. Ogawa, J. S. Godber, F. Shih, Random centroid optimization of phosphatidylglycerol stabilized lutein-enriched oil-in-water emulsions at acidic pH. *Food Chem.* **92**, 737–744 (2005).

19. S. Gurung, M. Holzer, S. Barnert, R. Schubert, Preparation and characterization of phospholipid stabilized nanoemulsions in small-scale. *bioRxiv* (2019), doi:10.1101/603803.

20. K. L. Saar, Y. Zhang, T. Müller, C. P. Kumar, S. Devenish, A. Lynn, U. Łapińska, X. Yang, S. Linse, T. P. J. Knowles, On-chip label-free protein analysis with downstream electrodes for direct removal of electrolysis products. *Lab Chip*. **18**, 162–170 (2018).

21. K. L. Saar, T. Muller, J. Charmet, P. K. Challa, T. P. J. Knowles, Enhancing the Resolution of Micro Free Flow Electrophoresis through Spatially Controlled Sample Injection. *Anal. Chem.* **90**, 8998–9005 (2018).

22. W. E. Arter, J. Charmet, J. Kong, K. L. Saar, T. W. Herling, T. Müller, U. F. Keyser, T. P. J. Knowles, Combining Affinity Selection and Specific Ion Mobility for Microchip Protein Sensing. *Anal. Chem.* **90**, 10302–10310 (2018).

23. B. D. Freibaum, J. P. Taylor, The Role of Dipeptide Repeats in C9ORF72-Related ALS-FTD. *Front. Mol. Neurosci.* **10**, 1–9 (2017).

24. S. Boeynaems, E. Bogaert, D. Kovacs, A. Konijnenberg, E. Timmerman, A. Volkov, M. Guharoy, M. De Decker, T. Jaspers, V. H. Ryan, A. M. Janke, P. Baatsen, T. Vercruysse, R.-M. Kolaitis, D. Daelemans, J. P. Taylor, N. Kedersha, P. Anderson, F. Impens, F. Sobott, J. Schymkowitz, F. Rousseau, N. L. Fawzi, W. Robberecht, P. Van Damme, P. Tompa, L. Van Den Bosch, Phase Separation of C9orf72 Dipeptide Repeats Perturbs Stress Granule Dynamics. *Mol. Cell*. **65**, 1044-1055.e5 (2017).

25. H. Baechtold, M. Kuroda, J. Sok, D. Ron, B. S. Lopez, A. T. Akhmedov, Human 75-kDa DNA-pairing protein is identical to the pro-oncoprotein TLS/FUS and is able to promote D-loop formation. *J. Biol. Chem.* **274**, 34337–34342 (1999).

26. N. E Farrawell, I. Lambert-Smith, S. Warraich, I. P Blair, D. Saunders, D. M Hatters, J. Yerbury, Distinct partitioning of ALS associated TDP-43, FUS and SOD1 mutants into cellular inclusions. *Sci. Rep.* **5**, 13416 (2015).

27. A. D. Efimova, R. K. Ovchinnikov, A. Y. Roman, A. V. Maltsev, V. V. Grigoriev, E. A. Kovrazhkina, V. I. Skvortsova, The FUS protein: Physiological functions and a role in amyotrophic lateral sclerosis. *Mol. Biol.* **51**, 341–351 (2017).

28. G. L. Dignon, W. Zheng, Y. C. Kim, R. B. Best, J. Mittal, Sequence determinants of protein phase behavior from a coarse-grained model. *PLoS Comput. Biol.* **14**, e1005941 (2018).

29. J. Kang, L. Lim, Y. Lu, J. Song, A unified mechanism for LLPS of ALS/FTLD-causing FUS as well as its modulation by ATP and oligonucleic acids. *PLOS Biol.* **17**, e3000327 (2019).

30. D. Zwicker, A. A. Hyman, F. Jülicher, Suppression of Ostwald ripening in active emulsions. *Phys. Rev. E - Stat. Nonlinear, Soft Matter Phys.* **92**, 012317 (2015).

31. M. R. White, D. M. Mitrea, P. Zhang, C. B. Stanley, D. E. Cassidy, A. Nourse, A. H. Phillips, M. Tolbert, J. P. Taylor, R. W. Kriwacki, C9orf72 Poly(PR) Dipeptide Repeats Disturb Biomolecular Phase Separation and Disrupt Nucleolar Function. *Mol. Cell*. **74**, 713-728.e6 (2019).

32. G. Urbina-Villalba, N. Garcia-Valera, K. Rahn-Chique, Theoretical Prediction and experimental measurement of the mixed flocculation/coalescence rate of ionic Hexadecane-in-water nano-emulsions. *arXiv* (2015) (available at https://arxiv.org/abs/1507.01116).

33. L. M. Jawerth, M. Ijavi, M. Ruer, S. Saha, M. Jahnel, A. A. Hyman, F. Jülicher, E. Fischer-

Friedrich, Salt-Dependent Rheology and Surface Tension of Protein Condensates Using Optical Traps. *Phys. Rev. Lett.* **121**, 258101 (2018).

34. M. Manciu, F. S. Manciu, E. Ruckenstein, On the surface tension and Zeta potential of electrolyte solutions. *Adv. Colloid Interface Sci.* **244**, 90–99 (2017).

35. W. Choi, U. Mahajan, S. M. Lee, J. Abiade, R. K. Singh, Effect of Slurry Ionic Salts at Dielectric Silica CMP. *J. Electrochem. Soc.* **151**, 185–189 (2004).

36. J. Stachurski, M. MichaŁek, The Effect of the ζ Potential on the Stability of a Non-Polar Oil-in-Water Emulsion. *J. Colloid Interface Sci.* **184**, 433–436 (1996).

37. N. C. Christov, A. Ganchev, N. D. Vassileva, N. D. Denkov, D. . Danov, K, P. A. Kralchevsky, Capillary mechanisms in membrane emulsification: oil-in-water emulsions stabilized by Tween 20 and milk proteins. *Colloids Surfaces A Physicochem. Eng. Asp.* **209**, 83–104 (2002).

38. W. M. Babinchak, R. Haider, B. K. Dumm, P. Sarkar, K. Surewicz, J.-K. Choi, W. K. Surewicz, The role of liquid-liquid phase separation in aggregation of the TDP-43 low complexity domain. *J. Biol. Chem.* **294**, 6306–6317 (2019).

39. Y. Lin, D. S. W. Protter, M. K. Rosen, R. Parker, Formation and Maturation of Phase-Separated Liquid Droplets by RNA-Binding Proteins. *Mol. Cell*. **60**, 208–219 (2015).

40. C. Weber, T. Michaels, L. Mahadevan, Spatial control of irreversible protein aggregation. *Elife*. **8**, e42315 (2019).

41. J. B. Woodruff, A. A. Hyman, E. Boke, Organization and Function of Non-dynamic Biomolecular Condensates. *Trends Biochem. Sci.* **43**, 81–94 (2018).

42. P. St George-Hyslop, J. Q. Lin, A. Miyashita, E. C. Phillips, S. Qamar, S. J. Randle, G. Wang, The physiological and pathological biophysics of phase separation and gelation of RNA binding proteins in amyotrophic lateral sclerosis and fronto-temporal lobar degeneration. *Brain Res.* **1693**, 11–23 (2018).

43. M. Garcia-Jove Navarro, S. Kashida, R. Chouaib, S. Souquere, G. Pierron, D. Weil, Z. Gueroui, RNA is a critical element for the sizing and the composition of phase-separated RNA–protein condensates. *Nat. Commun.* **10**, 3230 (2019).

44. S. Uppaluri, S. C. Weber, C. P. Brangwynne, Hierarchical Size Scaling during Multicellular Growth and Development. *Cell Rep.* **17**, 345–352 (2016).

45. M. Derenzini, D. Trerè, A. Pession, M. Govoni, V. Sirri, P. Chieco, Nucleolar size indicates the rapidity of cell proliferation in cancer tissues. *J. Pathol.* **191**, 181–186 (2000).

46. T. M. Franzmann, M. Jahnel, A. Pozniakovsky, J. Mahamid, A. S. Holehouse, E. Nüske, D. Richter, W. Baumeister, S. W. Grill, R. V. Pappu, A. A. Hyman, S. Alberti, Phase separation of a yeast prion protein promotes cellular fitness. *Science*. **359**, eaao5654 (2018).

47. A. Hernández-Vega, M. Braun, L. Scharrel, M. Jahnel, S. Wegmann, B. T. Hyman, S. Alberti, S. Diez, A. A. Hyman, Local Nucleation of Microtubule Bundles through Tubulin Concentration into a Condensed Tau Phase. *Cell Rep.* **20**, 2304–2312 (2017).

Figures

Figure 1.

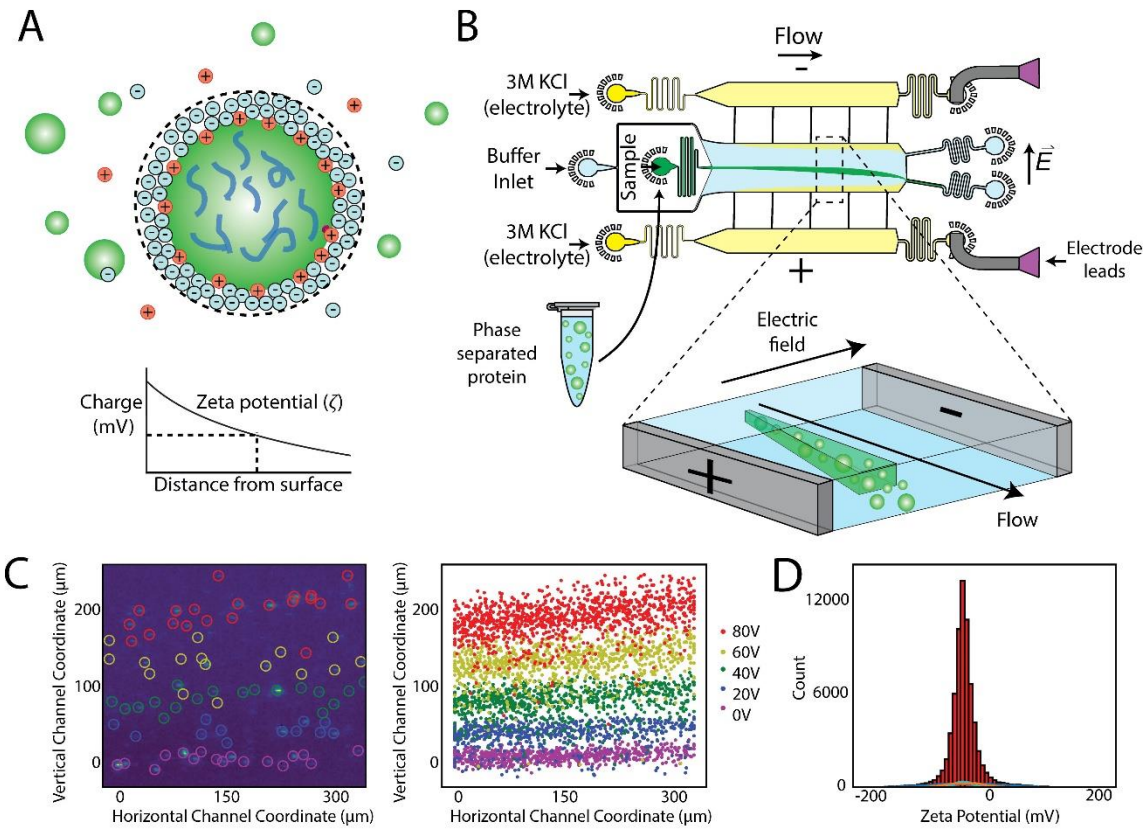

Figure 1: Overview of the microfluidic platform for quantifying single-condensate zeta potentials. (A) Schematic of the zeta potential of a protein condensate, which is the electrical potential at the edge of the ion layer surrounding a particle, denoted by the dashed lines. **(B)** Schematics of the µFFE device used to carry out the single-droplet zeta potential measurements. Phase separated droplets were introduced into the 3D free-flow electrophoresis device through a central injection port, preventing any contact between the condensates and the surface of the channel. The condensates were then deflected by applying a constant voltage and positions quantified as a measure of electrophoretic mobility to calculate zeta potentials. **(C)** Left panel: Overlaid images from multiple voltage applications in the range from 0–80 V, depicting individual protein condensates as they move through the image frame. Right panel: Tracked coordinates of detected condensates at each voltage in the range between 0 and 80 V; these coordinates were used to calculate the zeta potential (see Materials and Methods). **(D)** Each individual condensate was analyzed to yield single-droplet zeta potential distributions, represented as the sum of all obtained measurements across all voltages applied. Cityscapes at the bottom of each filled histogram are histograms derived from single voltage measurement.

Figure 2.

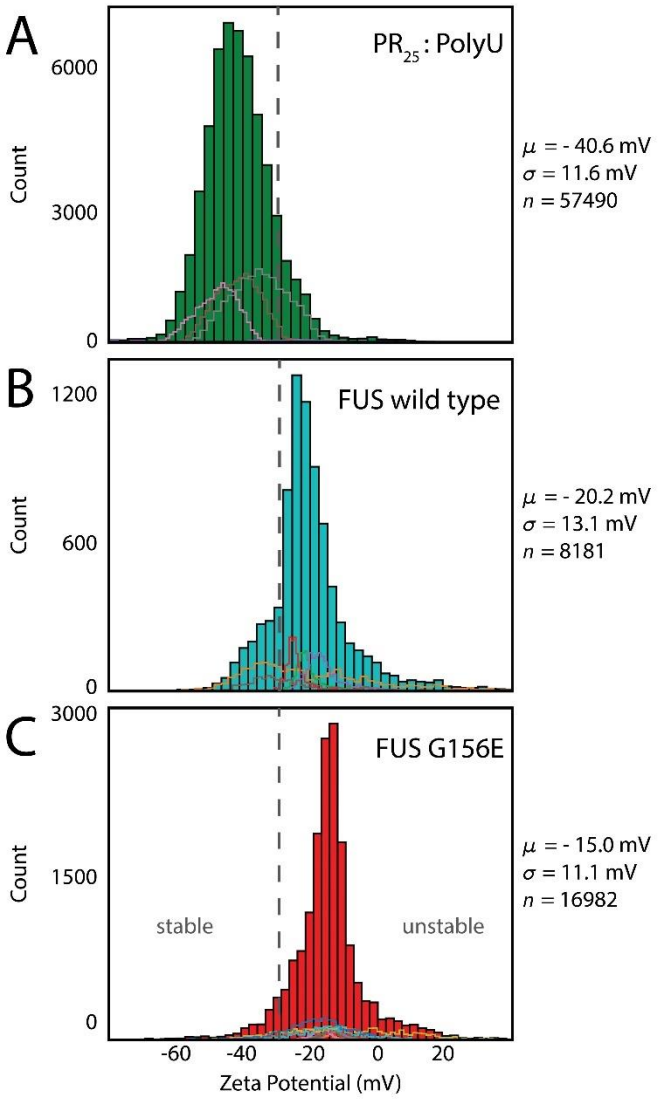

Figure 2: Single-droplet zeta potential measurements of biomolecular condensates. Histograms of single condensate zeta potential measurements for **(A)** PR_{25}:PolyU, **(B)** FUS wild type, and **(C)** FUS G156E condensates. Histograms were obtained from all measurements taken on a particular condensate system across all voltages applied, as illustrated in Figure 1. Solid line distributions in each panel at the bottom of each filled histogram represent a collection of measurements from a single replicate at a particular voltage value. Mean, μ, and width, σ, of distributions as well as number of droplets, n, probed are given. Dashed lines indicate boundaries for stable and unstable dispersion with zeta potential cut-offs at –30 mV (*17*, *19*).

Figure 3.

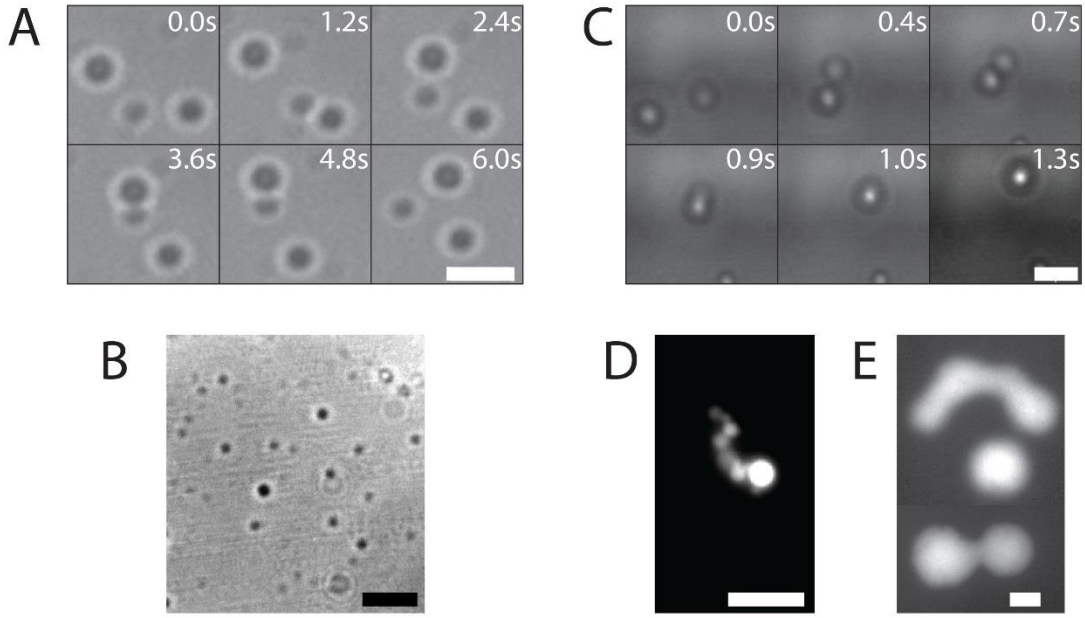

Figure 3: Observations of condensate stability from epifluorescence (Epi) and phase-contrast (PhC) microscopy. (A, B) Images of PR_{25}:PolyU (PhC), **(C,D)** FUS wild-type (PhC, Epi), and **(E)** FUS G156E (Epi) condensates. (A) PR_{25}:PolyU condensates are able to come into contact without fusing and (B) remain stable over many hours without fusing or clustering. (C) FUS wild-type condensates fuse rapidly in solution within seconds to minutes after mixing and (D) readily exhibit clustering behavior in solution. (E) Similarly, FUS G156E condensates rapidly fuse and wet glass surfaces within minutes after phase separation. All scale bars are 3 μm.

Figure 4.

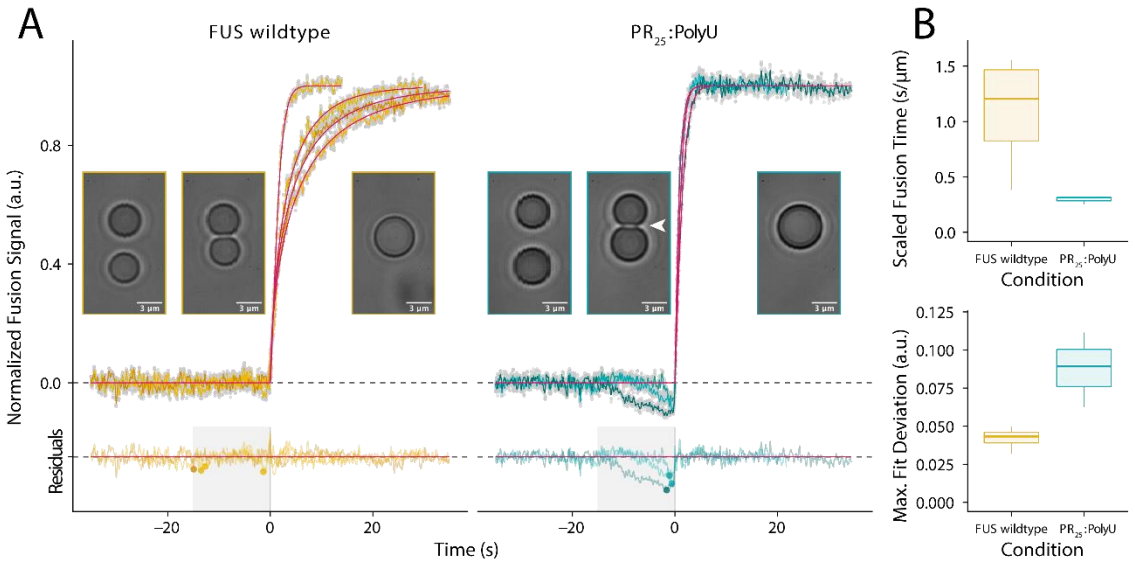

Figure 4: Assessment of condensate stability in controlled coalescence experiments. (**A**) Example traces of controlled droplet fusions using optical tweezers of FUS wild-type and PR_{25}:PolyU droplets, together with model fits (magenta) and corresponding residuals. 5% of the raw data (grey points) and smoothed signals (colored lines) are displayed for individual fusion events. For each condition, representative images before fusion, at the onset of fusion, and after fusion are shown. PR_{25}:PolyU droplets exhibited a clear indentation (white arrow) before fusion initiated. A significant deviation from the standard fusion model, as illustrated by the dip in the residuals, reflects an energy barrier to be overcome to induce PR_{25}:PolyU droplet fusion. We used a window of 15 seconds before fusion onset to quantify the maximum deviation from the model (colored data points). (**B**) Top panel: Size normalized relaxation times indicate that once initiated, PR_{25}:PolyU droplets fuse faster than FUS wild-type droplets. Bottom panel: Maximum deviation from the standard model serves as a proxy for the repulsive force required to start fusion.

Figure 5.

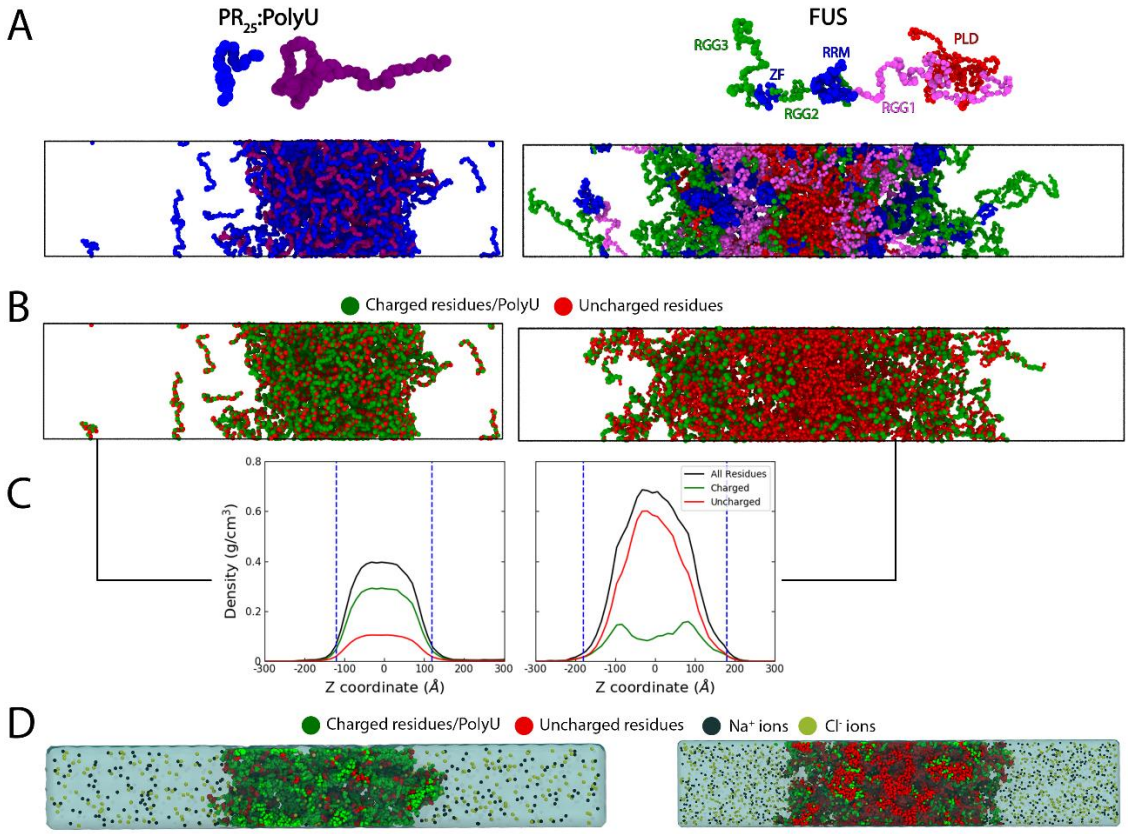

Figure 5: Molecular organization of PR_{25}:PolyU and FUS condensates. (A) Top panel: One-bead per amino acid/nucleotide coarse-grained representation of PR_{25} (blue), PolyU (purple) and FUS with the PLD (residues 1–165) in red, the extended arginine rich region 1 (RGG1; residues 166–284) in pink, the RNA-recognition motif (RRM; residues 285–371) and the Zinc Finger region (ZF; residues 423–453) in blue, the arginine rich regions 2 (RGG2; residues 372–422) and 3 (RGG3; residues 454–526) in green. Bottom panel: Representative coarse-grained equilibrium configurations obtained via direct coexistence molecular dynamics simulations (i.e., both liquid phases simulated in the same simulation box) of (left) PR_{25}:PolyU condensates showing homogeneous distribution of species, and (right) FUS with heterogeneous distribution of domains (see also Figure S5). **(B)** Representative configurations from A but with charged species (amino acids and PolyU) colored green and uncharged residues colored red. **(C)** Normalized density of charged and uncharged species across the long side of the simulation box estimated over the coarse-grained equilibrium ensemble showing a much higher concentration of charge in PR_{25}:PolyU. The vertical dashed lines show the location of the edge of the condensate. **(D)** Back-mapped atomistic system from equilibrium coarse-grained configuration used to estimate the differential behavior of ions in PR_{25}:PolyU and FUS condensates.

Supporting information for:

Single particle zeta-potential measurements reveal the role of electrostatics in protein condensate stability

Timothy J. Welsh[a,1], Georg Krainer[a,1], Jorge R. Espinosa[b,1], Jerelle A. Joseph[b], Akshay Sridhar[b], Marcus Jahnel[c,d,e], William E. Arter[a], Kadi L. Saar[a], Simon Alberti[d,*], Rosana Collepardo-Guevara[b,f,g,*], Tuomas P.J. Knowles[a,b,*]

[a] Centre for Misfolding Diseases, Department of Chemistry, University of Cambridge, Lensfield Road, Cambridge CB2 1EW, UK

[b] Cavendish Laboratory, University of Cambridge, J J Thomson Avenue, Cambridge CB3 0HE, UK

[c] Max Planck Institute of Molecular Cell Biology and Genetics, Pfotenhauerstr. 108, 01307 Dresden, Germany

[d] Biotechnology Center (BIOTEC), Center for Molecular and Cellular Bioengineering (CMCB), Technische Universität Dresden, Tatzberg 47/49, 01307 Dresden, Germany

[e] Cluster of Excellence “Physics of Life”, TU Dresden, Dresden, Germany

[f] Department of Genetics, University of Cambridge, Cambridge CB2 3EH, UK

[g] Department of Chemistry, University of Cambridge, Lensfield Road, Cambridge CB2 1EW, UK

* To whom correspondence may be addressed: Tuomas P.J. Knowles (tpjk2@cam.ac.uk), Rosana Collepardo-Guevara (rc597@cam.ac.uk), Simon Alberti (simon.alberti@tu-dresden.de)

[1] These authors contributed equally

Keywords: liquid–liquid phase separation, microfluidics, FUS, zeta potential, emulsion

Supporting Methods

Design of the µFFE device. The design of the µFFE microfluidic chip with liquid electrodes was adapted from a device previously used for studying protein charge and the separation of biomolecules (*1*, *2*). A schematic is shown in Figure S1. The device is 90 µm tall in the central electrophoresis chamber and 5 µm tall in the sample injection port. In total dimensions, the device is approximately 7 mm long and 2 mm wide. The 3D design was utilized to minimize the effect of velocity differences within the channel; further details on device design optimization are given in Saar *et al.* (*1*). For operation, the sample of interest containing phase-separated droplets is flown into the device by the central injection port where it is then surrounded by the carrier buffer solution, which was 5 mM Tris-HCl (pH 7.4) in experiments with PR_{25}:PolyU and 5 mM Tris-HCl (pH 7.4), 25 mM KCl in experiments with both FUS variants. On either side of the main channel, liquid electrolyte channels are filled with a constant flow of a 3 M KCl solution, supplemented with 1 mg/mL fluorescein (Sigma-Aldrich) for visualization purposes. The electrolyte solution enters the main channel via 40 µm wide and 5 µm tall electrolyte ridges, which allows for a narrow stream of electrolyte to coat both sides of the main electrophoresis channel. This solution remains under constant flow and acts as a liquid electrode, which is continually replaced. Utilization of liquid electrodes allows for high voltages to be applied as gaseous electrolysis products are flushed out of the device through the hollow electrodes (*3*). Further, the flow of electrolyte also aids in suppression of Joule heating within the device, which can be an issue with other types of micro-scale electrophoresis devices (*4*).

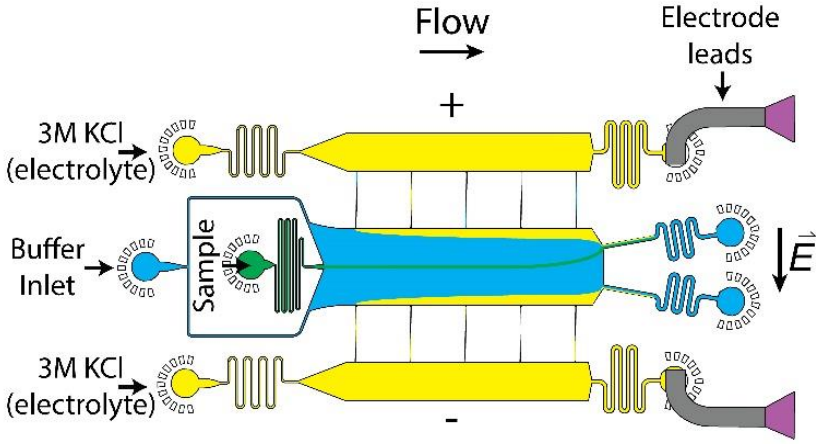

Figure S1: Full schematic of µFFE device. This schematic shows the general design of the 3D µFFE device. The sample is injected through a central port at the beginning of the channel, which is 5 µm tall. Thereby, the sample does not come into contact with any surfaces of the central channel containing co-flow buffer, which is 90 µm tall. The 3 M KCl solution acts as an electrolyte and flows along the edges of the central channel to allow the voltage to be transmitted from the outlet ports to the sample where an electric field is induced opposite to the direction of flow. Further description of the usage and design of the device is given in the text.

Fabrication of the µFFE device. Microfluidic masks were first designed using AutoCAD (Autodesk) and desired device geometries then printed on acetate transparencies (Micro Lithography Services). Polydimethylsiloxane (PDMS; DowCorning) devices were produced from SU-8 (MicroChem) molds fabricated via standard photolithographic processes by plasma bonding two individual PDMS chips to each other. Accordingly, two molds were made in order to comprise the two separate sides of the 3D microfluidic devices, with the bottom layer being produced from a single-layer (SL) replica mold, while the top layer was produced from a two-layer (TL) replica mold. Specifically, the mold for the SL chips was fabricated to a height of 45 µm and included all the structures of the devices with the exception of the protein inlet and the electrolyte bridges connecting the electrophoresis chamber and the electrolyte channels. This was achieved by spinning SU-8 3050 photoresist onto a polished silicon wafer (MicroChemicals) followed by standard soft-lithography procedures (*5*) using a custom-built LED based apparatus for performing the UV-exposure step (*6*). The fabrication of the TL replica mold for the top layer involved two subsequent lithography steps performed with SU-8 3005 and 3050 to obtain 5 and 45 µm high channels, respectively. The protein inlet as well as the connecting electrolyte bridges were featured only on the 5 µm layer, while the buffer inlet, the electrophoresis chamber, and the electrolyte channels were fabricated onto the 45 µm layer only are identical to how they appear on the SL replica mold. Feature heights on the master were assessed using a profileometer (DektakXT, Bruker). The top and bottom layer replica molds were then used to fabricate PDMS chips employing a 10:1 prepolymer-PDMS-to-curing-agent ratio (Sylgard 184, DowCorning). After degassing and curing for 3 h at 65°C, the two halves of the devices were then cut out of the molds, and holes for tubing connection (0.75 mm) and electrode insertion (1.5 mm) were created in the top layer PDMS half. Both sides of the devices were cleaned by application of Scotch tape and sonication in isopropanol. Following treatment using an oxygen plasma oven (Femto, Diener electronic) at 40% power for 30 s, the PDMS bottom layer was bonded on a glass slide with the channels facing upward. The PDMS top layer was then placed on top and carefully aligned to create a 3D device. The device was baked at 65°C for 24 h to ensure optimal bonding. Before use, devices were rendered hydrophilic via prolonged exposure to oxygen plasma (500 s, 80% power) (*7*). After this treatment, surface hydrophilicity was prolonged by immediate filling of device channels with deionized water using gel-loading tips (Fisherbrand).

Device operation and experimental conditions in µFFE experiments. The device was operated by injecting the sample solution, the carrier buffer solution, and the electrolyte solution into the corresponding inlets using automated syringe pumps (neMESYS, Cetoni). The sample was introduced from a 100 µL glass syringe (Hamilton), other solutions were flowed from 10 mL plastic Norm-Ject syringes (Henke-Sass Wolf). All fluids were introduced to the device by 0.012X0.030" PTFE tubing (Cole-Parmer). Typical values for the flow rates were 5 µL/hr for the sample, 400–500 µL/hr for the carrier medium, and 100–250 µL/hr for the electrolyte solutions. Fluid waste was

guided out of the device by tubing inserted into device outlets. Electric potentials were applied using a programmable 500 V power supply (Elektro-Automatik EA-PS 9500-06) via bent hollow metal dispensing tips (15G, Intertonics) inserted into the electrolyte outlets. The voltage was varied in linear steps, typically in the range between 0 to 80 V, using a computer controller (Raspberry Pi). Simultaneously, current readings using a digital multimeter (34401A, Agilent Technologies) were taken. Schematics of the electrical setup can be seen in Figure S2. The measurements for determining the electrical resistance of the electrodes and estimating the effective electrical potential applied across the devices were performed in an identical manner but with the sample and carrier medium replaced with 3 M KCl solution as has been described in detail earlier. All measurements were performed at room temperature.

Optical detection in μFFE experiments. Images were acquired using an inverted fluorescence microscope (Zeiss AxioObserver D1) equipped with a high-sensitivity electron-multiplying charge-coupled device (EMCCD) camera (Evolve 512, Photometrics). In experiments with FUS, an appropriate filter set for EGFP detection was used (49002, Chroma Technology). Exposure times were around ~10 ms for each image, allowing for between 30–100 particles to be imaged per frame, and 500–2000 to be imaged per experimental μFFE run. Due to high amounts of free PR_{25} monomer in solution, images for the PR_{25} system were captured in bright-field mode with a phase contrast ring (Ph2). The movement of the droplets in the microfluidic chip was collected by running samples containing the phase-separated droplets into the main chamber of the device and taking images approximately at the coordinate corresponding to the 4th electrolyte bridge (i.e., approx. after 4 s of travel within the chip). At each voltage, a series of images were taken in order to detect ~500–2000 droplets.

Data analysis and calculation of zeta potentials. Images taken in μFFE experiments were analyzed using the Fiji/ImageJ data processing software. Condensates were detected using the TrackMate package (*8*), which returned the x,y-coordinates of individual droplets within the channel, with x being the coordinate in the direction of the length of the channel (i.e., flow direction) and y being the coordinate in the direction of its width (i.e., perpendicular to the flow). By calibrating the position of the image within the channel, the travelled distance in x,y-direction over a stream of images was determined, which subsequently gave the residence time, t_r, needed for drift velocity calculations (i.e., the lateral and longitudinal movement of droplets in time). Accordingly, the drift velocity, v, was calculated from the vertical displacement of each condensate, referred to as Δy, according to

$$v = \frac{\Delta y}{t_r}$$

Δy is quantified as the vertical displacement of each condensate from the average vertical coordinate of the stream at 0 V, and t_r was calculated from the flow rate, the x coordinate (or

distance traveled), and the known dimensions of the channel. Note, given that the sample stream height is <5% of the height of the total channel and the co-flow buffer flow rate is 50 times higher than the sample flow rate, not much broadening of the signal from the parabolic flow profile is to be expected, which would occur mainly near the edges of the device and may cause velocity variations across the channel.

With v at hand, the electrophoretic mobility, μ, was calculated as

$$\mu = \frac{v}{E_{\text{eff}}}$$

where E_{eff} is the effective electric field across the main electrophoresis channel. E_{eff} is equivalent to V_{eff}/w, with V_{eff} being the effective voltage and w being the width of the device, and was obtained through calibration of each device with 3 M KCl as shown in Figure S2B.

In order to determine V_{eff}, first the resistances R were determined according to Ohm's law $R = V/I$ for each point shown in Figure S2B. By filling the device with 3 M KCl, the internal resistance is effectively zero; therefore, the resistance of the electrode, $R_{\text{elect}} = V_{\text{app}}/I$, could be determine from the 3 M KCl calibration measurement. Similarly, the resistance of the entire device could be determined during the sample measurement according to the relation, $R_{\text{dev}} = V_{\text{app}}/I$.

With the resistances R_{elect} and R_{dev} at hand, the resistance of only the internal measurement chamber could be calculated as $R_{\text{main}} = R_{\text{dev}} - R_{\text{elect}}$. Thereby, the voltage drop within the main chamber, expressed as a percentage drop could be calculated as the ratio $eff_V = R_{\text{main}}/R_{\text{dev}}$. Typically, electrical resistances of 115 and 100 kΩ were determined for R_{dev} and R_{elect}, respectively, and we obtained voltage efficiencies varying from 2% to 12%. From this, V_{eff} could be calculated according to $V_{\text{eff}} = eff_V \times V_{\text{app}}$, where V_{app} is the applied voltage at the respective sample measurement. This allowed E_{eff} to be determined and therefore the mobility μ of the droplets to be calculated as described.

The measured electrophoretic mobilities for each condensate could then be converted into the zeta potential, ζ, according to the following relation using a modified version of Henry's function (*9*)

$$\zeta = \frac{\mu\eta}{\varepsilon\varepsilon_0}$$

In this relation, ε is relative permittivity of the solution, ε_0 is the permittivity of a vacuum, and η is the dynamic viscosity of the solution. The solution was treated as water, thus the accepted value of $\varepsilon = 78.5$ (*10*) and $\eta = 1.0518\text{x}10^{-3}$ Pa s (*11*) were used. All calculations were all carried out in Python using the integrated development environment Spyder.

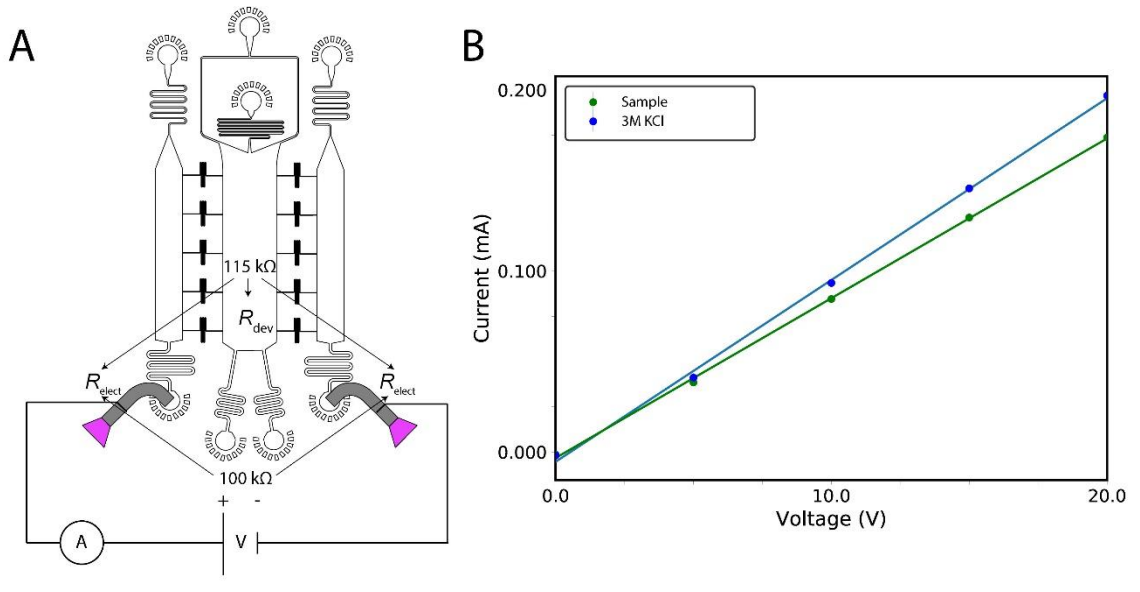

Figure S2: Electrical circuit and calibration of device. (A) Circuit schematic displays how the voltage is applied across the μFFE device and indicates the two sources of voltage drop (high electrical resistance), the electrodes (R_{elect}) and the device itself (R_{dev}). **(B)** Plot displaying the electrical current transmitted through the device both with the sample present (green) and when the device was filled with 3 M KCl solution (blue). Error bars of three measurements at each voltage are smaller than the marker size. This plot allows for the calibration of the voltage efficiency as described in the text.

Supporting Results

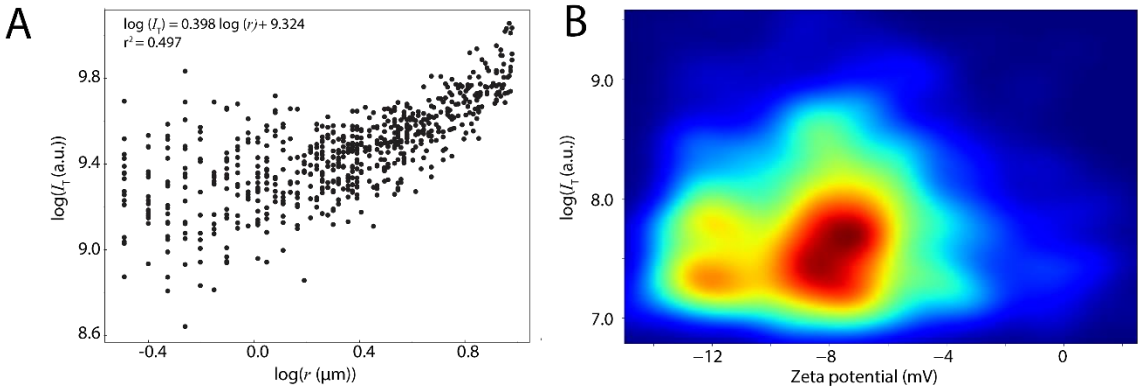

Figure S3: Size dependence of zeta potential. (A) Log–log plot of radius, r, versus total fluorescence intensity, I_T, of individual FUS condensates at 6 µM FUS in 50 mM TRIS-HCl at pH 7.4 and 50 mM KCl. r and I_T were detected with the TrackMate package in the FIJI image processing software on still images. The correlation between r and I_T of the condensates was fitted with a log model. **(B)** 2D plot of zeta potential versus I_T of individual FUS condensates. The plot shows that condensates with varying zeta potentials have similar distributions of I_T, indicating a lack of correlation between zeta potential and size of condensates.

Size dependence of zeta potential. The size of the condensates could not be determined from µFFE experiments because condensates were under flow and appeared blurred in the images due to the 10 ms exposure time. Thus, the size versus zeta potential relationship had to be derived by secondary means. First, static epifluorescence images of FUS condensates were taken. This analysis showed that there is a weak correlation between the total fluorescence intensity (I_T) and the radius (r) of FUS condensates (Figure S3A). In a second step, I_T and zeta potential were derived from images taken during µFFE experiments (Figure S3B). Building on the weak correlation between I_T and r, these data suggest that is no correlation between the zeta potential and I_T, thus indicating that there is no correlation between size and zeta potential.

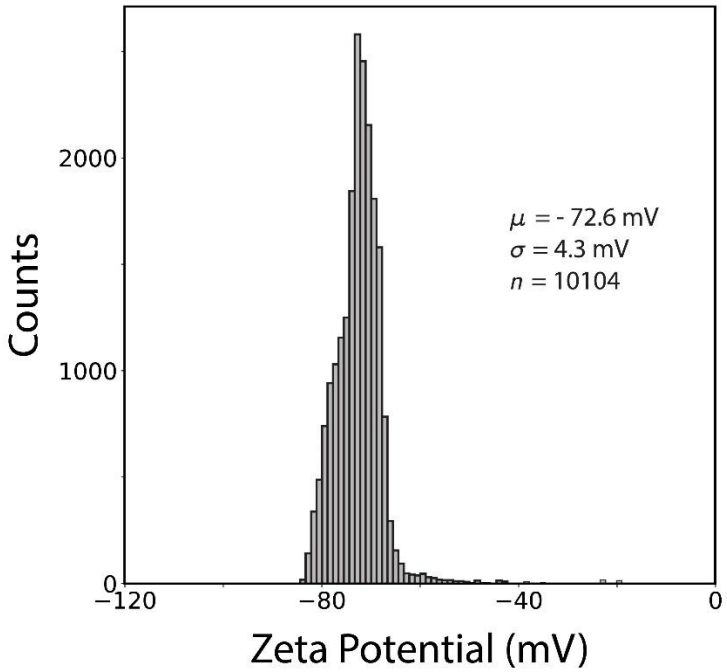

Figure S4: Zeta potential measurement of 60 nm gold nanoparticles. The zeta potential of monodispersed 60 nm gold nanoparticles were measured using the same 3D microfluidic method as for protein condensate measurements.

Colloid control measurements. As a control, the zeta potential of 60 nm gold nanoparticles was analyzed using the same microfluidic method as for protein condensate measurements. It was observed that the zeta potential distribution of gold nanoparticles is narrow compared to the distribution of condensates, with the relative standard deviation amounting to only 8% and 20% of that of protein samples. Moreover, there were less broad tails to the distribution in the nanoparticles, which is consistent with the fact that the nanoparticles are monodisperse in size and composition. Note that the nanoparticles are at least an order of magnitude smaller than the condensate systems studied here; hence, due to diffusion effects, the width of the zeta potential distribution of 60 nm gold nanoparticles is likely broader than that of monodisperse particles which are similar in size as condensates.

Supporting Computational Methods

Coarse-grained protein model. To model the condensation of FUS and PR_{25}, we used the sequence-dependent coarse-grained model of the Mittal group (*12*), which treats each amino acid residue as a single bead. Intrinsically disordered regions were modeled as flexible polymers, with inter-residue bonds described using a harmonic potential. Globular regions were treated as rigid bodies. A Coulombic term with Debye–Hückel electrostatic screening was used for long-range electrostatics, while a knowledge-based potential, termed HPS, that is based on a hydrophobicity scale for amino acids found in the literature (*13*) was used to describe pairwise hydrophobic interactions. We have scaled down the set of HPS parameters by 30% to account for the 'buried' amino acids contained in the globular "rigid" domains.

Initial atomistic models for coarse-grained simulations. We modelled the full length FUS protein based on Unitprot code K7DPS7 (526 residues, 24 proteins) and a reduced version of the PR_{25} protein (12 Arg and 13 Pro residues alternately positioned, 200 proteins). We developed an atomistic model of FUS by attaching the disordered regions to the resolved structural domains (residues 285–371 (PDB code: 2LCW) and residues 422–453 (PDB code: 6G99)). Initial intrinsically disordered models for PR25 were developed in PyMol (*14*).

Minimal coarse-grained model for PolyU. We modelled PolyU (30 strands of 80 nucleotides each) as a flexible polymer that represents each nucleotide as a single bead. Inter-residue bonds were described using a rigid harmonic spring, and long-range electrostatics were modelled using a Coulombic term with Debye–Hückel electrostatic screening plus dispersive interactions. Each bead was assigned a charge of –1 and the HPS set of parameters for Glu dispersive interactions.

Coarse-grained simulation methods. We performed direct coexistence simulations at constant volume and temperature to describe the formation of liquid condensates in the different systems. The direct coexistence method consists of simulating both the condensate and diluted phases in the same box separated by an interface. These initial simulation boxes containing both phases were prepared by running simulations at constant temperature and a pressure of 1 bar, using the Berendsen barostat, and then enlarging the simulation box in one direction ~3.5 times. The simulation temperatures were chosen to be below the correspondent critical temperatures of each system: 280K for full length FUS and 440 K for PR_{25} with ssRNA. We ran ~2 μs of MD simulations using a Langevin thermostat with relaxation time of 5 ps and a time step of 10 fs (*15*). The LAMMPS software MD package was used to carry out all the coarse-grained simulations (*16*).

Back-mapping from coarse grained to atomistic scale. Starting from equilibrium coarse-grained structures of the condensates we built atomic resolution systems following a three-step procedure. Step 1: We unwrapped the coarse-grained bead coordinates across the periodic boundaries and

defined the unwrapped bead positions as coordinates for the amino-acid Cα atoms. Using the tleap module of Amber16 (*17*), we added the missing sidechain and backbone atoms in random orientations. Step 2: Because adding atoms in this way results in significant atomic overlaps that cannot be resolved through standard energy minimization procedures, we mapped these atomistic configurations to the higher-resolution coarse grained model Martini (*18*) and standard Martini Water (*19*). For nucleic acids, the 'soft' Martini parameters (*20*) without elastic bonds were used. The system was then energy minimized in the Martini resolution for 5000 steps using the steepest descent algorithm. Step 3: Finally, the program "backward" (*21*) was then used to backmap the Martini configuration to the atomistic resolution.

Atomistic Molecular Dynamics Simulations. After back-mapping, we solvated the atomistic condensates using the Gromacs 2018 command gmx solvate (*22*) with the modified TIP3P water model (*23*) creating a rectangular box with the long side (*z*-direction) being 12.5 nm away from the condensate interface. We then added Na^+/Cl^- ions at an initial concentration of 0.2 M using the parameters of Beglov and Roux (*24*) together with the nbfix changes of Luo and Roux (*25*) and Venable et al. (*26*). We used the Charmm36M force field (*27*, *28*), which is one of the standard force field combinations for proteins and nucleic acids in explicit solvent and ions. For the FUS system, this resulted in a system of dimensions 12x12x65 nm with 24 protein molecules (170'160 atoms), 250'095 water molecules, and 900 Na^+ and 1236 Cl^- ions. For the PR_{25}:PolyU system, this resulted in a system of dimensions 7x7x52 nm with 45 protein molecules (21'285 atoms), 14 PolyU chains (40 nucleotides, 17'906 atoms), 76'885 water molecules , and 283 Na^+ and 277 Cl^- ions.

MD simulations were performed with Gromacs 2018 (*22*) using the SETTLE algorithm (*29*) to constrain bond lengths and angles of water molecules and P-LINCS for all other bond lengths, which allowed for a time step of 2 fs to numerically integrate the equations of motions. Temperatures were maintained at 300 K using the v-rescale thermostat (*30*) and the pressure at 1 bar using the Parrinello-Rahman barostat (*31*). Long range electrostatic interactions were calculated using the Particle Mesh Ewald (PME) algorithm (*32*) with a cut-off of 1.0 nm. We first perform a short 25-ns long pre-equilibration MD simulation, then after absorption of ions into the condensed phase, the concentration of ions in the diluted phase was verified and adjusted back to 0.2 M (moles of NaCl per liter of solution) by addition/removal of ions or water molecules. We then conducted a 150 ns long MD simulation to investigate the distribution of ions within the condense and diluted phases. The trajectories were analyzed using a combination of Gromacs tools and Python MDAnalysis scripts (*33*). For the calculation of partial densities of atoms across the long box axis, the Cα atoms of the system were first centered within the box and the *density* module of Gromacs was used. For the calculation of interaction preferences, two residues were assumed to be in contact if the minimum distance between their constituent atoms was <3.0 Å in the atomistic resolution and 6.5 Å in the CG resolution. For the calculation of domain interactions, the contacts

of all the domain's constituent residues were summed and normalized by the domain's length. The trajectories were visualized using VMD (*34*) Pymol (*14*) and Ovito (*35*).

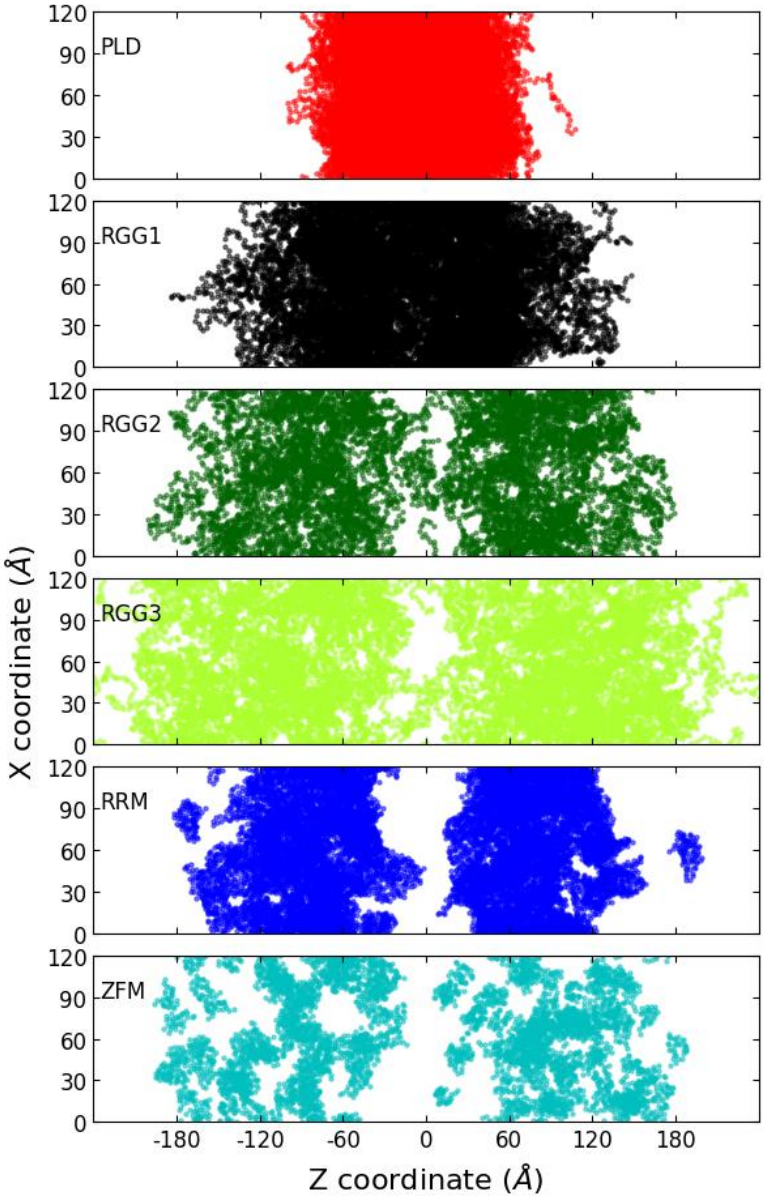

Figure S5: Two-dimensional projection of FUS trajectories showing the positional distribution of FUS domains within the condensate. A separate plot is shown for each of the different domains of FUS, with PLD (residues 1–165) in red, extended arginine rich region 1 (RGG1; residues 166–284) in black, arginine rich region 2 (RGG2; residues 372–422) in green, the arginine rich region 3 (RGG3; residues 454–526) in light green, RNA-recognition motif (RRM; residues 285–371) in blue, and Zinc Finger region (ZF; residues 423–453) in cyan. The dots in each plot represent the collection of amino-acid bead positions sampled in our simulations projected on the x/z plane to ease visualization.

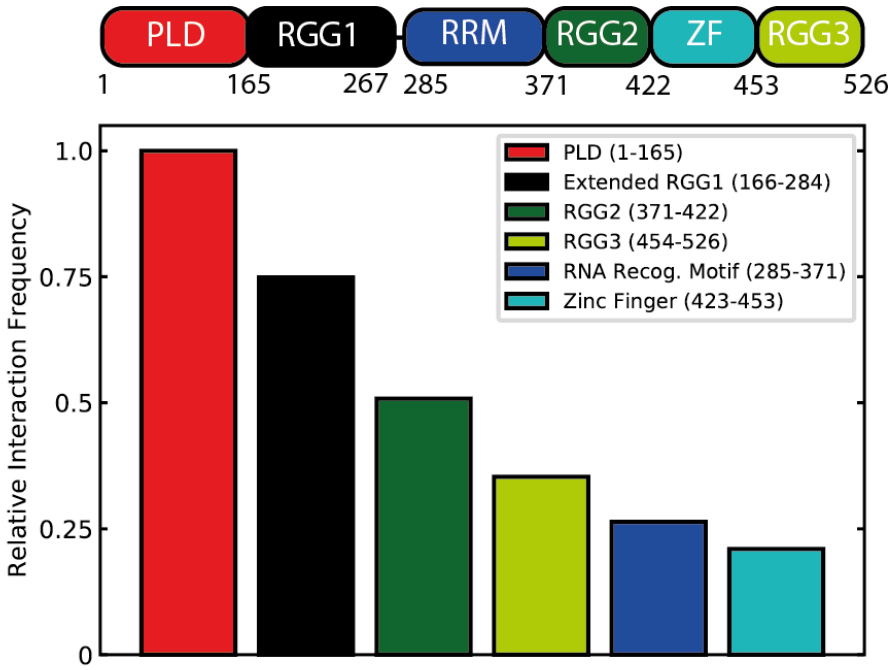

Figure S6: Contact maps showing the relevance of inter-region interactions for the formation of biomolecular condensates in FUS. The bars show the number of inter-protein contacts (amino acids closer than a cut-off of 0.65 nm) mediated by each FUS region normalized by the maximum number of contacts among regions.

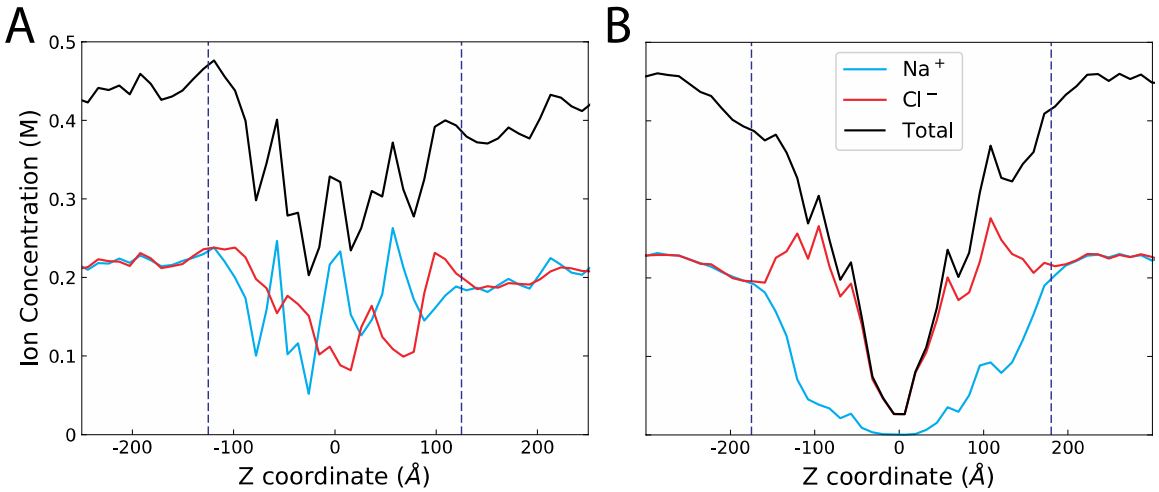

Figure S7: (A) Equilibrium concentration of Na^+ (cyan), Cl^- (red), and total Na^+ + Cl^- ions (black) PR_{25}:PolyU and **(B)** FUS systems estimated from atomistic direct coexistence MD simulations in which both the diluted and condensed phases are simulated in the same box separated by an interface. The vertical dashed lines show approximately the location of the condensate interfaces (condensates are positioned in the center and are in contact with a surrounding diluted phase). The simulations were prepared ensuring equal equilibrium concentrations of ions in the diluted phases for both systems. In such conditions, the concentration of ions inside PR_{25}:PolyU condensates is higher than in FUS.

Table S1: To estimate the differential behavior of ions in and around FUS and PR_{25}:PolyU condensates, we measured diffusion coefficients of ions in the condensed ($D_{condensate}$) versus the diluted phase ($D_{diluted}$) for both systems. The values are calculated from a linear fit of the Mean Square Displacements (MSD) exhibited by the different ions in each phase. The time intervals for the calculation of diffusion coefficients (10 ns) was chosen as the longest interval that minimized intermixing of ions in the condensed phase with ions in the diluted phase. The error estimates are calculated as the difference in diffusion coefficients obtained from two time intervals.

System	Ions	$D_{condensate}$ (10^{-5} cm^2/s)	$D_{diluted}$ (10^{-5} cm^2/s)	Mobility Ratio $\left(D_{condensate}/D_{diluted}\right)$
PR_{25}:PolyU	Na^+	0.866 ± 0.34	2.269 ± 0.15	0.38
	Cl^-	1.080 ± 0.37	2.983 ± 0.66	0.36
FUS	Na^+	1.046 ± 0.23	2.220 ± 0.24	0.47
	Cl^-	1.190 ± 0.15	2.788 ± 0.16	0.42

Supporting References

1. K. L. Saar, Y. Zhang, T. Müller, C. P. Kumar, S. Devenish, A. Lynn, U. Łapińska, X. Yang, S. Linse, T. P. J. Knowles, On-chip label-free protein analysis with downstream electrodes for direct removal of electrolysis products. *Lab Chip*. **18**, 162–170 (2018).

2. W. E. Arter, J. Charmet, J. Kong, K. L. Saar, T. W. Herling, T. Müller, U. F. Keyser, T. P. J. Knowles, Combining Affinity Selection and Specific Ion Mobility for Microchip Protein Sensing. *Anal. Chem.* **90**, 10302–10310 (2018).

3. K. L. Saar, T. Muller, J. Charmet, P. K. Challa, T. P. J. Knowles, Enhancing the Resolution of Micro Free Flow Electrophoresis through Spatially Controlled Sample Injection. *Anal. Chem.* **90**, 8998–9005 (2018).

4. T. W. Herling, T. Müller, L. Rajah, J. N. Skepper, M. Vendruscolo, T. P. J. Knowles, Integration and characterization of solid wall electrodes in microfluidic devices fabricated in a single photolithography step. *Appl. Phys. Lett.* **102**, 184102 (2013).

5. Y. Xia, G. M. Whitesides, Soft lithography. *Annu. Rev. Mater. Sci.* **28**, 153–184 (1998).

6. P. K. Challa, T. Kartanas, J. Charmet, T. P. J. Knowles, Microfluidic devices fabricated using fast wafer-scale LED-lithography patterning. *Biomicrofluidics*. **11**, 014113 (2017).

7. S. H. Tan, N. T. Nguyen, Y. C. Chua, T. G. Kang, Oxygen plasma treatment for reducing hydrophobicity of a sealed polydimethylsiloxane microchannel. *Biomicrofluidics*. **4**, 32204 (2010).

8. J. Y. Tinevez, N. Perry, J. Schindelin, G. M. Hoopes, G. D. Reynolds, E. Laplantine, S. Y. Bednarek, S. L. Shorte, K. W. Eliceiri, TrackMate: An open and extensible platform for single-particle tracking. *Methods*. **115**, 80–90 (2017).

9. J. W. Swan, E. M. Furst, A simpler expression for Henry's function describing the electrophoretic mobility of spherical colloids. *J. Colloid Interface Sci.* **388**, 92–94 (2012).

10. C. G. Malmberg, A. A. Maryott, Dielectric constant of water from 0 to 100 C. *J. Res. Natl.*

Bur. Stand. (1934). **56**, 2641 (1956).

11. J. Kestin, M. Sokolov, W. A. Wakeham, Viscosity of liquid water in the range -8°C to 150°C. *J. Phys. Chem. Ref. Data*. **7**, 941–948 (1978).

12. G. L. Dignon, W. Zheng, Y. C. Kim, R. B. Best, J. Mittal, Sequence determinants of protein phase behavior from a coarse-grained model. *PLoS Comput. Biol.* **14**, e1005941 (2018).

13. L. H. Kapcha, P. J. Rossky, A simple atomic-level hydrophobicity scale reveals protein interfacial structure. *J. Mol. Biol.* **426**, 484–498 (2014).

14. Schrödinger, LLC, "The {PyMOL} Molecular Graphics System, Version~1.8" (2015).

15. J. S. Rowlinson and B. Widom, *Molecular Theory of Capillarity* (Clarendon Press, Oxford, 1984).

16. S. Plimpton, Fast parallel algorithms for short-range molecular dynamics. *J. Comput. Phys.* **117**, 1–19 (1995).

17. D. A. Case, T. E. Cheatham, T. Darden, H. Gohlke, R. Luo, K. M. Merz, A. Onufriev, C. Simmerling, B. Wang, R. J. Woods, The Amber biomolecular simulation programs. *J. Comput. Chem.* **26**, 1668–1688 (2005).

18. L. Monticelli, S. K. Kandasamy, X. Periole, R. G. Larson, D. P. Tieleman, S. J. Marrink, The MARTINI coarse-grained force field: Extension to proteins. *J. Chem. Theory Comput.* **4**, 819–834 (2008).

19. S. O. Yesylevskyy, L. V. Schäfer, D. Sengupta, S. J. Marrink, Polarizable water model for the coarse-grained MARTINI force field. *PLoS Comput. Biol.* **6**, 1–17 (2010).

20. J. J. Uusitalo, H. I. Ingólfsson, P. Akhshi, D. P. Tieleman, S. J. Marrink, Martini Coarse-Grained Force Field: Extension to DNA. *J. Chem. Theory Comput.* **11**, 3932–3945 (2015).

21. T. A. Wassenaar, K. Pluhackova, R. A. Böckmann, S. J. Marrink, D. P. Tieleman, Going backward: A flexible geometric approach to reverse transformation from coarse grained to atomistic models. *J. Chem. Theory Comput.* **10**, 676–690 (2014).

22. M. J. Abraham, T. Murtola, R. Schulz, S. Páll, J. C. Smith, B. Hess, E. Lindah, Gromacs: High performance molecular simulations through multi-level parallelism from laptops to supercomputers. *SoftwareX*. **1**–**2**, 19–25 (2015).

23. J. Huang, S. Rauscher, G. Nawrocki, T. Ran, M. Feig, B. L. De Groot, H. Grubmüller, A. D. MacKerell, CHARMM36m: An improved force field for folded and intrinsically disordered proteins. *Nat. Methods*. **14**, 71–72 (2016).

24. D. Beglov, B. Roux, Finite representation of an infinite bulk system: Solvent boundary potential for computer simulations. *J. Chem. Phys.* **100**, 9050 (1994).

25. Y. Luo, B. Roux, Simulation of osmotic pressure in concentrated aqueous salt solutions. *J. Phys. Chem. Lett.* **1**, 183–189 (2010).

26. R. M. Venable, Y. Luo, K. Gawrisch, B. Roux, R. W. Pastor, Simulations of anionic lipid membranes: Development of interaction-specific ion parameters and validation using NMR data. *J. Phys. Chem. B*. **123**, 9066–9079 (2013).

27. K. Hart, N. Foloppe, C. M. Baker, E. J. Denning, L. Nilsson, A. D. MacKerell, Optimization of the CHARMM Additive Force Field for DNA: Improved Treatment of the BI/BII Conformational Equilibrium. *J. Chem. Theory Comput.* **8**, 348–362 (2011).

28. E. J. Denning, U. D. Priyakumar, L. Nilsson, A. D. MacKerell, Impact of 2′-hydroxyl sampling on the conformational properties of RNA: Update of the CHARMM all-atom additive force field for RNA. *J. Comput. Chem.* **32**, 1929–1943 (2011).

29. S. Miyamoto, P. A. Kollman, Settle: An analytical version of the SHAKE and RATTLE algorithm for rigid water models. *J. Comput. Chem.* (1992), doi:10.1002/jcc.540130805.

30. G. Bussi, D. Donadio, M. Parrinello, Canonical sampling through velocity rescaling. *J. Chem. Phys.* **126**, 014101 (2007).

31. M. Parrinello, A. Rahman, Polymorphic transitions in single crystals: A new molecular dynamics method. *J. Appl. Phys.* **52**, 7182 (1981).

32. U. Essmann, L. Perera, M. L. Berkowitz, T. Darden, H. Lee, L. G. Pedersen, A smooth particle mesh Ewald method. *J. Chem. Phys.* **103**, 8577 (1995).

33. N. Michaud-Agrawal, E. J. Denning, T. B. Woolf, O. Beckstein, MDAnalysis: A toolkit for the analysis of molecular dynamics simulations. *J. Comput. Chem.* **32**, 2319–2327 (2011).

34. W. Humphrey, A. Dalke, K. Schulten, VMD: Visual molecular dynamics. *J. Mol. Graph.* **14**, 33–38 (1996).

35. A. Stukowski, Visualization and analysis of atomistic simulation data with OVITO-the Open Visualization Tool. *Model. Simul. Mater. Sci. Eng.* **18**, 015012 (2010).